Derivation and Implementation of the Seismic Image Wave Theory and its Application to Seismic Reflection Data

Diploma thesis
by
Jürgen Mann

(English version)

Geophysical Institute
University of Karlsruhe

19th March 1998

Preface

In September 1997 I completed my master thesis (*Diplomarbeit*) titled *Herleitung und Implementierung der Seismic-Image-Wave-Theorie und Anwendung auf reflexionsseismische Meßdaten*. As usual and quite obvious I wrote it in German, but meanwhile I had to realize that this is more disadvantageous than I had expected. Considering the encouraging interest in my thesis, I decided to translate it. I request the reader to ignore the linguistic mistakes I made during the translation—you will still recognize the German style...

Abstract

This thesis is concerned with the derivation, implementation and application of the seismic image wave theory by Hubral et al. [HTS96]. In this theory, well-known imaging problems are taken as wave propagation phenomena with appropriate propagation variables. The theory is partly generalized to 3D in this thesis. The seismic image wave theory is based on the method of discontinuities by Goldin [Gol90], [Gol89].

Based on straightforward geometrical approaches, image wave equations are derived for four different imaging problems: post-stack remigration in the time domain, post-stack remigration in the depth domain, migration to zero-offset (MZO, and dip moveout (DMO). The latter two problems are self-explanatory and are also called configuration transforms by Hubral et al. [HST96] and Tygel et al. [TSH96]. Post-stack remigration means transforming images migrated with a (possibly wrong) velocity model to a new image corresponding to another (updated) velocity model.

In the present thesis, the derivations are restricted to constant velocity models and the kinematical aspects of the imaging problems. The basic idea is to chain migration and demigration methods to obtain so-called Huygens image waves for the respective imaging problem. This is closely related to the unified approach to 3D seismic reflection imaging by Hubral et al. [HST96] and Tygel et al. [TSH96], where Kirchhoff-type operators are introduced for the mentioned imaging problems.

Using the Huygens image waves, corresponding image wave eikonal equations are derived. I propose four seismic image wave equations which can be shown to yield the mentioned image wave eikonal equations by using ansatzes similar to the well-known zero-order ray approximation. While the proposed MZO and DMO image wave equations are restricted to 2D and were already presented by Hubral et al. [HTS96], the image wave equations for the remigration problems are generalized to 3D.

The imaging problems may now be reformulated as initial value problems (IVP). In the framework of this thesis, these IVP are solved by using semi-explicit finite difference (FD) schemes. The FD schemes and some additional features are implemented and provide the following range of possibilities:

- *2D and 3D remigration in the time and depth domain applied towards higher or lower velocities.*
- *Normal moveout for constant velocity models.*
- *DMO and MZO for an arbitrary number of common-offset gathers.*
- *Stacking of DMO or MZO results.*

The FD schemes are applied to various synthetic and real data sets. Apart from the MZO, which has not yet produced useful results, all imaging problems are successfully solved by this implementation. In particular the remigration in the time domain and the DMO proved very stable.

These methods allow one to see the seismic images propagating through the respective domain when changing the respective propagation variable, i. e. offset or velocity. Thus the sensitivity of the images to parameter changes may be observed. Please note that the propagation takes place in fictitious domains and does not correspond to any physical propagation processes. For obvious reasons, these methods are also called velocity and offset continuation, resp.

With remigration, the best image can be selected out of a sequence of many by observing the changes of significant structures in the images, like bow ties or diffraction patterns. Structures of this kind are used to determine an optimum constant migration velocity, i. e. to obtain information on the macro velocity model. Although derived for a constant velocity model, remigration in the time domain also proves applicable to weakly inhomogeneous models with certain restrictions, as is shown for the Marmousi 3D overthrust model.

As remigration in time domain accepts (simulated) zero-offset data associated with the migration velocity $v = 0$*, the implemented methods may be chained in order to obtain time-migrated images from pre-stack data by subsequently using NMO, DMO, stack and remigration in the time domain.*

Contents

Chapter 1

Introduction

The present thesis deals with the derivation, implementation and application of the seismic image wave theory by Hubral et al. [HTS96]. Within the scope of this theory, we conceive four well-known seismic imaging problems as generalized wave propagation phenomena. The theory is based on the method of discontinuities by Goldin [Gol90], [Gol89].

This chapter embraces four sections: firstly, we introduce the imaging problems under consideration. In the second section we discuss some properties of the physical wave propagation which will be transfered to the seismic imaging problems in the third section. Finally, the last section describes the basic structure of this thesis.

First of all some definitions: emphasized parts of the text are printed in *slant* letters, the names of programs and program packages in sans serif, and names of hardware devices are printed in SMALL CAPITALS. These definitions partly collide with the style parameters for headings and page headers. Therefore, they, cannot be used in all situations. The abbreviations 1D, 2D and 3D should be read as adjectives (”two dimensional”) or as nouns with number (”two dimensions”) depending on the respective context.

1.1 The imaging problems

In the present thesis we consider four different imaging problems: remigration in the time domain, remigration in the depth domain, migration to zero-offset (MZO), and the dip moveout (DMO) correction. The two remigration problems are applied to post-stack data, the other imaging problems to pre-stack data.

The remigration in the time or depth domain enables us to transform an image migrated with a (possibly wrong) velocity model to a new migrated image corresponding to another (improved) velocity model. There is no need to access the original unmigrated data set for this process, but only the already migrated image is required. It should be mentioned that the migration velocity $v = 0$ is associated with the (simulated) zero-offset section in the

time domain.

Remigration is a generalization of the residual migration by Rothman et al. [RLR85] and the cascaded migration by Larner et al. [LB87]. These methods are restricted to small changes of the velocity model while the remigration is not restricted in this respect. The 2D equations proposed by Hubral et al. [HTS96] are generalized to 3D in this thesis.

A classical approach to simulate zero-offset sections is to chain a normal moveout (NMO) correction and a DMO followed by a stacking of the simulated zero-offset sections. The NMO corrects the influence of the offset for horizontal reflectors but yields wrong images of dipping reflectors. The DMO subsequently considers the influence of the dip on the traveltimes. The MZO, however, performs the same as chained NMO and DMO in one single processing step.

In this context we understand a common-offset data set as a section recorded along a straight acquisition line. Shots and receivers are always situated on the acquisition line, MZO and DMO are pure 2D problems accordingly. Anyway, it is possible to simulate a 3D zero-offset data set by applying MZO or DMO to several parallel lines successively.

Depending on the respective propagation variable we also designate the mentioned methods velocity or offset continuation methods, respectively.

1.2 Physical wave propagation

This discussion is confined to the propagation of body waves in acoustic media. The propagation of seismic energy in such media is described by a linear partial differential equation of second order. Representing the wavefield by the pressure $p(t,\vec{x})$ at all locations $\vec{x}$ at the time t, the wave propagation can be simulated by solving the initial value problem $p_0 = p(t = t_0, \vec{x}) \rightarrow p = p(t,\vec{x})$.

A long time before the scalar wave equation was found, several simple principles were already used to describe some aspects of the wave propagation phenomenon, namely the Fermat's principle and the conceptions of elementary or Huygens waves, wavefronts, and rays.

The conception of Huygens waves and wavefronts is of particular significance for the seismic image wave theory. A wavefront represents a purely kinematical property of the wavefield, namely the location of a discontinuity in the wavefield. An elementary or Huygens wave is simply a wavefront emitted by a point source.

Using the Huygens waves, we can construct a wavefront at time t_2 by taking each point on a known wavefront for t_1 as point source of a Huygens wave. The envelope of all Huygens wavefronts after the time $t_2 - t_1$ is the searched-for wavefront.

The Huygens wave can be derived from the scalar wave equation with a ray-theoretical

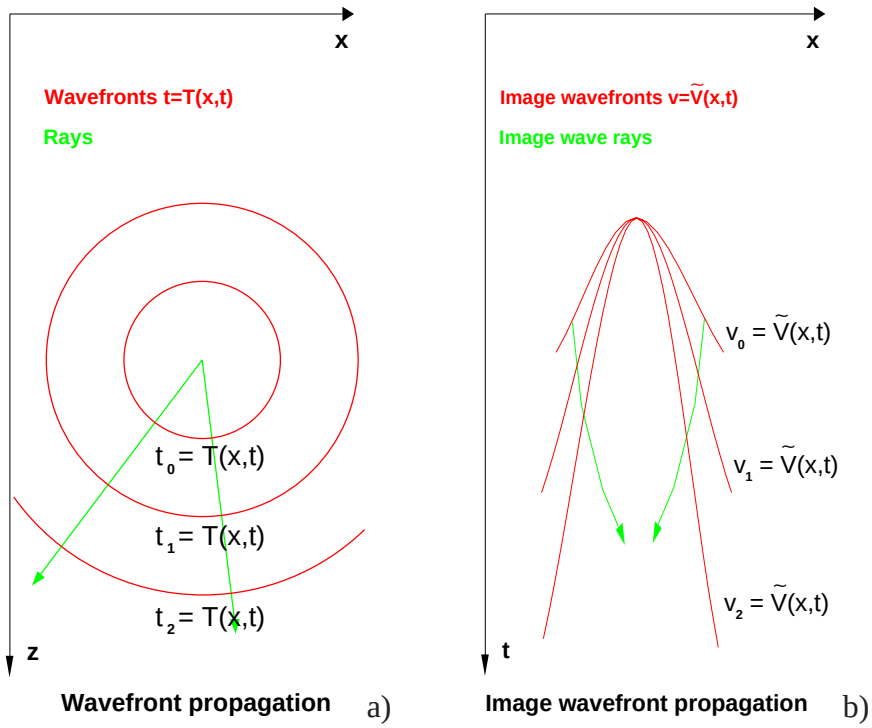

Figure 1.1: a) Rays and wavefronts in a homogeneous acoustic medium, b) time-migrated images of a point for different constant velocities. Some wavefronts are partly shown.

ansatz of zeroth order or an ansatz similar to equation (2.1): this yields the so-called eikonal equation, a non-linear partial differential equation of first order. The solution of the eikonal equation is the Huygens wave. Vice versa, the eikonal equation can be derived from the Huygens wave. The eikonal is a parameterized representation of a wavefront for a fixed time t.

1.3 Seismic image waves

The transition to seismic image waves may be illustrated with an example for one of the four imaging problems under consideration: in fig. 1.1a we have snapshots of a wavefront in a homogeneous acoustic medium for three different moments. For the sake of simplicity, we consider a point source. In fig. 1.1b we have different time-migrated images of one and the same point in a seismic section for three different constant velocities.

Now, we take the different images in fig. 1.1b as wavefronts of a propagation phenomenon. The propagation variable is problem-specific, in this example it is the velocity v. This view is sheerly abstract and not related to any physical propagation process. The figure also includes the according image wave rays which, however, are not relevant for this thesis.

As already mentioned, wavefronts in an acoustic medium can be constructed by using the

Huygens principle. Now, we transfer this method to the seismic imaging problems: each point on the—in this particular case migrated—image for the velocity v_1 in fig. 1.1b is taken as a source point of a Huygens wave. The envelope of all Huygens waves after the "time" $v_2 - v_1$ is the wavefront, i. e. the searched-for image, for the velocity v_2.

The same strategy can be applied to all the imaging problems mentioned above. For MZO and DMO the respective propagation variable is obviously the offset. In the framework of this thesis we only consider homogeneous[1] isotropic media for the derivations.

We can calculate the Huygens waves for the imaging problems under consideration by a chained application of migration and demigration (or vice versa). This procedure is identical with the unified approach to 3D seismic reflection imaging by Hubral et al. [HST96] and Tygel et al. [TSH96]. The authors derived Kirchhoff-type operators for different seismic imaging problems.

Introducing parameterized representations of the image wavefronts, the so-called eikonals, we can derive the according eikonal equations from the Huygens waves.

For each imaging problem and its related eikonal equation we propose an image wave equation. Using ansatzes similar to the zero-order ray approximation for physical waves in acoustic media, these image wave equations yield the derived eikonal equations.

This ensures that at least the kinematical properties of the considered imaging problems can be described by the proposed image wave equations. The imaging problems may now be rewritten as initial value problems with—depending on the particular imaging problem—the velocity or the offset as propagation variable, respectively.

We solve the initial value problems by means of semi-explicit finite difference (FD) schemes. The implementations based on this approach are finally applied to various synthetic and real data sets. The implementation of the DMO and MZO additionally includes an NMO correction and the option to stack the simulated zero-offset sections.

1.4 Structure of the thesis

Starting with straightforward geometrical considerations, we calculate the Huygens waves for the four imaging problems in chapter 2. Using the parameterized wavefronts, i. e. the eikonals, the associated eikonal equations are derived. These eikonal equations describe the kinematical aspects of the imaging problems. Finally, we propose image wave equations for all imaging problems which also yield the derived eikonal equations if we insert appropriate ansatzes. We compare the results with the well-known case of physical wave propagation.

Chapter 3 deals with the discretization and implementation of the image wave equations as well as with the implementation of the NMO correction and the stacking procedure.

[1] I.e. homogeneous with respect to the velocity—the density may vary.

The application of the remigration in the time and depth domain is extensively discussed in chapter 4.

In chapter 5 we discuss the application of the NMO/DMO and the MZO to several synthetic data sets.

Finally we conclude the results in chapter 6.

Chapter 2

Seismic image wave theory

2.1 The scalar wave equation

The principle of seismic image wave methods is based on treating the imaging problems with the same formalism like the scalar wave equation, although there is no physical propagation process related to them.

This formalism includes the idea of wavefronts which can be taken as envelopes of elementary or Huygens waves, which, on the other hand, are solutions of the eikonal equation. This eikonal equation, a non-linear partial differential equation of first order, describes the kinematical aspects of the wave propagation. The entire wave field is described by the wave equation, a linear partial differential equation of second order.

The scalar wave equation also describes the dynamical properties of the (physical) wavefield, whereas the seismic image wave methods are restricted to the purely kinematical properties of the image wave field in the framework of this thesis.

To emphasize the large analogy of physical wave propagation and seismic image waves, we derive the eikonal equation from the scalar wave equation with the ansatz

$$p(\vec{x},t) = p_0(\vec{x})\, f\left[t - T(\vec{x})\right] . \tag{2.1}$$

In this equation, $t = T(\vec{x})$ represents the propagating wavefront, $p_0(\vec{x})$ the initial wavefield, and f is an arbitrary smooth function. In media with constant density, the scalar or acoustic wave equation in 3D reads

$$\nabla^2 p(\vec{x},t) = \frac{1}{v^2}\frac{\partial^2}{\partial t^2} p(\vec{x},t) , \tag{2.2}$$

with v as propagation velocity within the medium. After inserting the ansatz (2.1) into the wave equation (2.2) we obtain

$$f'' p_0 \left[(\nabla T)^2 - \frac{1}{v^2} \right] - f' \left(2\nabla p_0 \cdot \nabla T + p_0 \nabla^2 T \right) + f \nabla^2 p_0 = 0 . \tag{2.3}$$

To satisfy this equation for any arbitrary function f, each of the terms with f'', f' and f must vanish separately. The resulting three equations

$$(\nabla T)^2 - \frac{1}{v^2} = 0\,, \tag{2.4}$$

$$2\nabla p_0 \cdot \nabla T + p_0 \nabla^2 T = 0 \tag{2.5}$$

and

$$\nabla^2 p_0 = 0 \tag{2.6}$$

contain only two scalar functions $p_0(\vec{x})$ and $T(\vec{x})$. Therefore, the problem is overdetermined. In a high frequency approximation we can neglect the term with f, i. e. equation (2.6). The remaining equations are the so-called eikonal equation (2.4) and the so-called transport equation (2.5).

Whereas the transport equation (2.5) depends on the entire wavefield p_0, the eikonal equation (2.4) contains no corresponding terms. Hence, it follows that the eikonal equation only describes the kinematical properties of the propagations process, but not the amplitudes of the wavefield.

In a homogeneous medium with $v = const$ the solution of the eikonal equation (2.4) reads

$$t = T(\vec{x}) = t_0 + \frac{|\vec{x} - \vec{x}_0|}{v}\,. \tag{2.7}$$

It describes the kinematical aspects of an elementary or Huygens wave with concentric spherical wavefronts centered in the source point $\vec{x}_0$.

The explained classical method starts with the well-known scalar wave equation (2.2), leading to the eikonal equation and the Huygens wave. In seismic image wave theory, however, the respective image eikonal and image wave equations first have to be derived. That is why we have to examine the reversibility of the method:

The eikonal equation (2.4) can be easily derived from the Huygens wave (2.7) by applying the gradient operator:

$$\nabla T(\vec{x}) = \frac{1}{v}\frac{\vec{x} - \vec{x}_0}{|\vec{x} - \vec{x}_0|} \tag{2.8}$$

Squaring the equation (2.8), which describes the rays penetrating the wavefront $T(\vec{x})$, immediately yields the desired result.

2.2 Remigration in the depth Domain

To obtain the eikonal equation for the remigration in the depth domain, we proceed as follows: we demigrate each point (x_0, y_0, z_0) on a reflector Σ_0 into the time domain with the velocity v_0. In the case of the simplest acquisition geometry, it is the zero-offset configuration. The coincident shot and receiver pairs are situated in the acquisition plane $z = 0$ and

are given by the coordinates (ξ,η). For a homogeneous model we immediately obtain the traveltime surface in the time domain, a hyperboloid reading

$$t(\xi,\eta) = \frac{2}{v_0}\sqrt{(x_0-\xi)^2+(y_0-\eta)^2+z_0^2}. \tag{2.9}$$

The envelope of all traveltime surfaces for all reflector points (x_0,y_0,z_0) is the zero-offset traveltime surface corresponding to the reflector Σ_0.

Each point $M(\xi,\eta,t)$ on the hyperboloid (2.9) is now migrated back into the depth domain with another velocity $v \neq v_0$. The isochron for each of these points is a half-sphere with the radius $vt/2$ centered at $(\xi,\eta,0)$:

$$t^2 = \frac{4}{v^2}\left[(x-\xi)^2+(y-\eta)^2+z^2\right] \tag{2.10}$$

The entire family of isochrons for all points on the hyperboloid for a fixed point (x_0,y_0,z_0) is obtained by squaring equation (2.9) and subsequent equating with the isochron equation (2.10). In this way we obtain an implicit function

$$F(x,y,z,\xi,\eta) = (x-\xi)^2+(y-\eta)^2+z^2-\frac{v^2}{v_0^2}\left[(x_0-\xi)^2+(y_0-\eta)^2+z_0^2\right] = 0 \tag{2.11}$$

parameterized by the point of acquisition (ξ,η). The envelope of this family of curves is defined by the two conditions $\partial F/\partial\xi = 0$ and $\partial F/\partial\eta = 0$. With these conditions we can calculate the parameter pairs (ξ,η) for which F is stationary:

$$\xi = \frac{1}{1-\frac{v^2}{v_0^2}}\left(x-\frac{v^2}{v_0^2}x_0\right) \tag{2.12}$$

$$\eta = \frac{1}{1-\frac{v^2}{v_0^2}}\left(y-\frac{v^2}{v_0^2}y_0\right) \tag{2.13}$$

Inserting the equations (2.12) and (2.13) into the implicit formula of the family of isochrons (2.11), we finally obtain the envelope of the family of isochrons (2.14). By analogy with the Huygens waves for the scalar wave equation, we call this envelope the Huygens image wave for depth remigration:

$$z = \frac{v}{v_0}\sqrt{z_0^2+\frac{(x-x_0)^2+(y-y_0)^2}{1-\frac{v^2}{v_0^2}}} \tag{2.14}$$

The construction of the Huygens image wave for one fixed velocity is shown in fig. 2.1a. The figure is reduced to 2D, because it would be quite confusing in 3D. Snapshots of the Huygens image wave in 2D are shown in fig. 2.1b. Finally we show the construction of an image wavefront for a reflector migrated with a (possibly wrong) velocity v_0 in fig. 2.2.

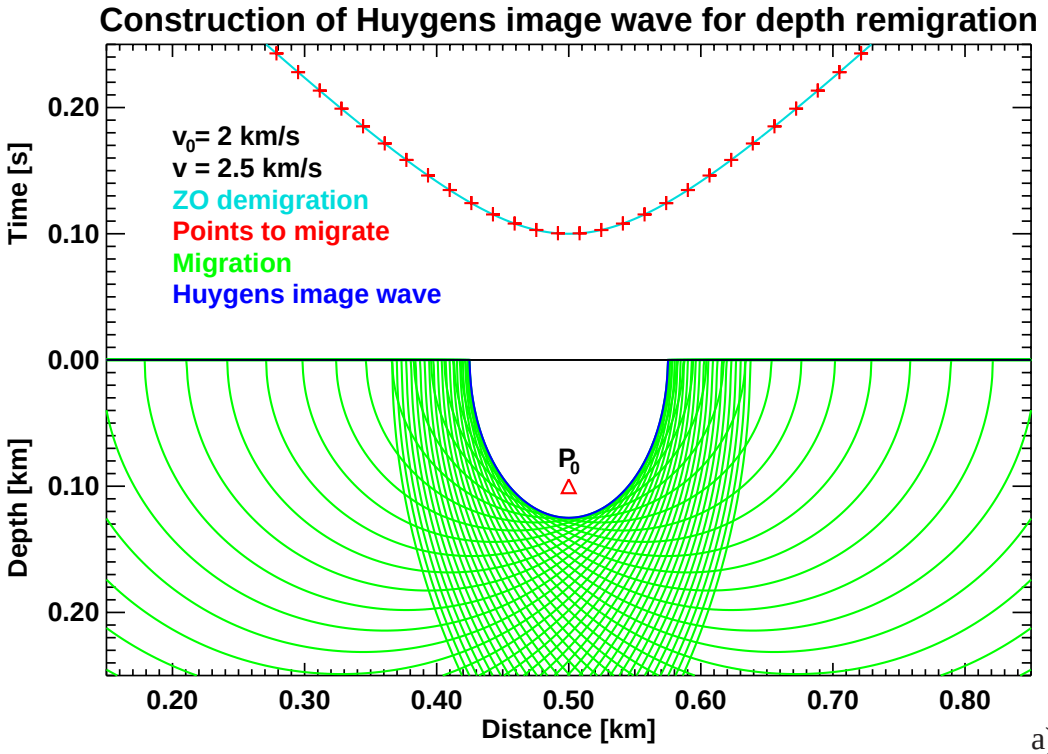

a)

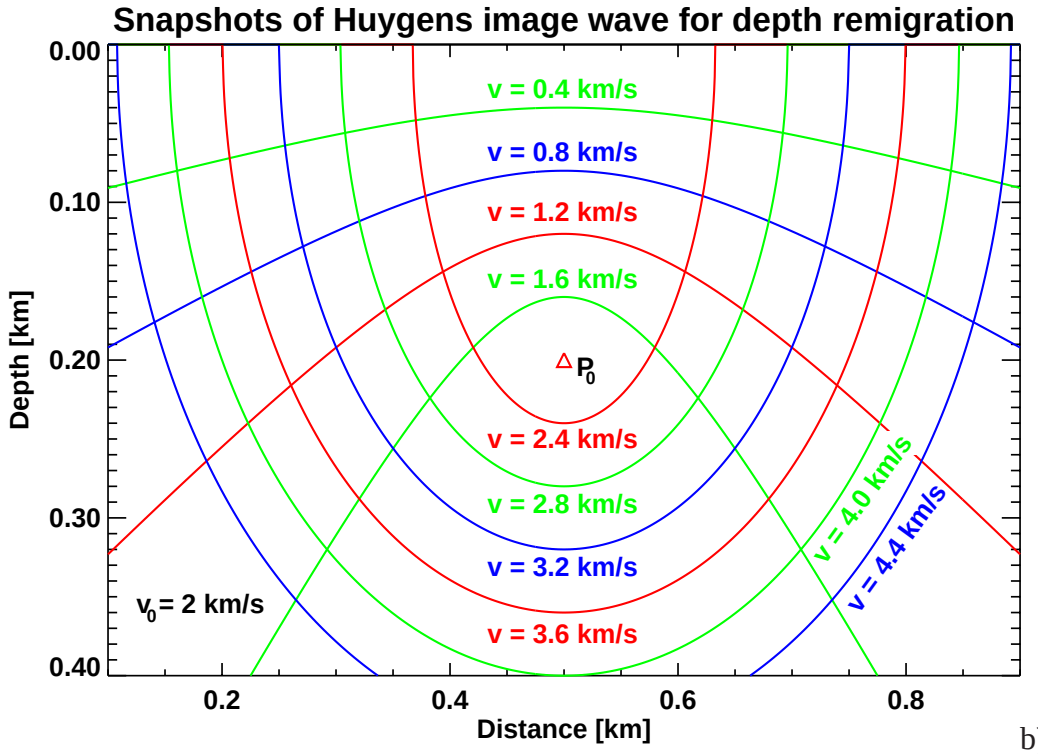

b)

Figure 2.1: a) Construction of the exploding Huygens wave for the remigration in the depth domain, b) snapshots of the Huygens wave for different velocities.

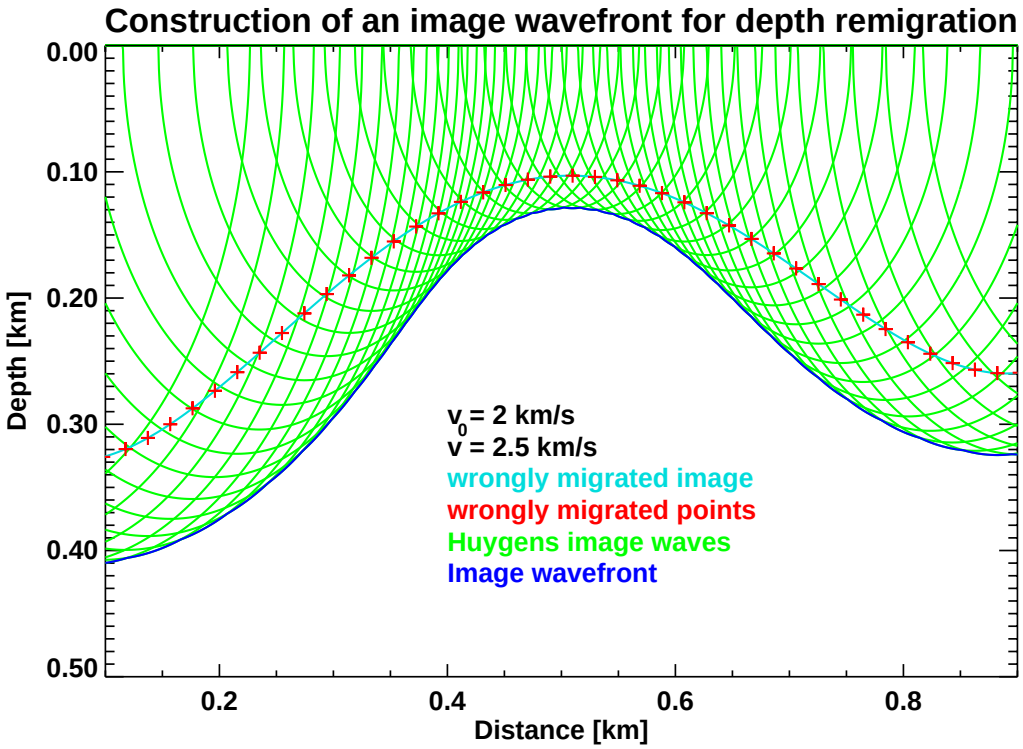

Figure 2.2: Construction of an image wavefront for the remigration in the depth domain.

To obtain an equation for the eikonal $v = V(x,y,z)$, we insert it into the Huygens image wave (2.14). A subsequent substitution $M(x,y,z) = V(x,y,z)/v_0$ simplifies the notation and leads to

$$z = M(x,y,z)\sqrt{z_0^2 + \frac{(x-x_0)^2 + (y-y_0)^2}{1-M^2(x,y,z)}}\,. \tag{2.15}$$

Now, we calculate the derivatives of equation (2.15) with respect to x, y and z. Squaring and adding the two derivatives with respect to x and y yields

$$\begin{aligned} 0 \;=\; & \left[\sqrt{z_0^2 - \frac{(x-x_0)^2+(y-y_0)^2}{1-M^2}} + \frac{M^2\left[(x-x_0)^2+(y-y_0)^2\right]}{(1-M^2)^2\sqrt{z_0^2+\frac{(x-x_0)^2+(y-y_0)^2}{1-M^2}}}\right]^2 \\ \times \; & \left(M_x^2+M_y^2\right) - \frac{M^2\left[(x-x_0)^2+(y-y_0)^2\right]}{(1-M^2)^2\left[z_0^2+\frac{(x-x_0)^2+(y-y_0)^2}{1-M^2}\right]}\,, \end{aligned} \tag{2.16}$$

whereas the derivative with respect to z, divided by M_z and squared, yields the following:

$$\frac{1}{M_z^2} = \left[\sqrt{z_0^2 - \frac{(x-x_0)^2+(y-y_0)^2}{1-M^2}} + \frac{M^2\left[(x-x_0)^2+(y-y_0)^2\right]}{(1-M^2)^2\sqrt{z_0^2+\frac{(x-x_0)^2+(y-y_0)^2}{1-M^2}}}\right]^2 \tag{2.17}$$

Inserting (2.17) into (2.16) we obtain

$$0 = \frac{\left(M_x^2 + M_y^2\right)}{M_z^2} - \frac{M^2\left[(x-x_0)^2 + (y-y_0)^2\right]}{(1-M^2)^2\left[z_0^2 + \frac{(x-x_0)^2+(y-y_0)^2}{1-M^2}\right]} \tag{2.18}$$

and finally we insert the equation (2.15), divided by M and squared:

$$\frac{z^2}{M^4}\frac{M_x^2 + M_y^2}{M_z^2} = \frac{(x-x_0)^2 + (y-y_0)^2}{(1-M^2)^2} \tag{2.19}$$

Inserting equation (2.19) into equation (2.17) and inserting z/M according to equation (2.15) yields the eikonal equation for $M(x,y,z)$

$$M_x^2 + M_y^2 + M_z^2 - \frac{MM_z}{z} = 0\,. \tag{2.20}$$

After resubstituting $V(x,y,z) = v_0 M(x,y,z)$ into equation (2.20) we obtain the eikonal equation for $V(x,y,z)$:

$$V_x^2 + V_y^2 + V_z^2 - \frac{VV_z}{z} = (\nabla V)^2 - \frac{V}{z}\frac{\partial V}{\partial z} = 0 \tag{2.21}$$

Now, we use a vector notation to obtain a more compact representation of the image wave equation and the proposed ansatz.

If we reduce the problem to two dimensions the derived eikonal equation (2.21) gets equivalent to the equation derived by Hubral et. al [HTS96][1]. On the analogy of the image wave equation

$$\frac{\partial^2 p}{\partial x^2} + \frac{\partial^2 p}{\partial z^2} + \frac{v}{z}\frac{\partial^2 p}{\partial z \partial v} = 0 \tag{2.22}$$

for two dimensions proposed in the same paper, we propose a more general image wave equation in 3D:

$$\nabla^2 p + \frac{v}{z}\frac{\partial^2 p}{\partial z \partial v} = 0 \tag{2.23}$$

In the same way we used the ansatz (2.1) for the scalar wave equation, we now use the ansatz

$$p(\vec{x}, v) = p_0(\vec{x})\, f[v - V(\vec{x})]\,. \tag{2.24}$$

In the following, we demonstrate that this ansatz also leads to the derived eikonal equation (2.21). Inserting the ansatz (2.24) into the proposed image wave equation, we obtain

$$f'' p_0 \left[(\nabla V)^2 - \frac{v}{z}\frac{\partial V}{\partial z}\right] + f'\left(\frac{v}{z}\frac{\partial p_0}{\partial z} - \nabla p_0 \cdot \nabla V - p_0 \nabla^2 V\right) + f\left(\nabla^2 p_0 - \nabla p_0 \cdot \nabla V\right) = 0\,. \tag{2.25}$$

To be satisfied for any arbitrary function f, the expressions with f, f' and f'' must vanish separately. In a high frequency approximation we only consider the first term of equation

[1] The cited paper contains a wrong sign in equation (A7): the third term should be positive, too.

(2.25). If we substitute the eikonal $V(x,y,z)$ for v we immediately obtain the eikonal equation (2.21) derived above.

According to this, the image wave equation (2.23) describes the kinematical properties of the remigration in the depth domain. However, we cannot make any statement related to the amplitudes of the wavefield. The remigration in the depth domain may now be rewritten as initial value problem:

$$p(v = v_0, \vec{x}) \rightarrow p(v, \vec{x}) \tag{2.26}$$

2.3 Remigration in the time domain

In the time domain we can apply the same strategy to derive the eikonal equation as in the depth domain. Since we consider a homogeneous model $v = const$, the straightforward transformation

$$\left(x_0, y_0, \frac{2z_0}{v_0}\right) \rightarrow (x_0, y_0, t) \tag{2.27}$$

from the depth to the time domain may be used. This enables us to refer to results already derived in the depth domain. Starting point is the Huygens image wave (2.14) in the depth domain. Transforming it into the time domain according to equation (2.27) we obtain

$$t = \sqrt{t_0^2 + \frac{4\left[(x-x_0)^2 + (y-y_0)^2\right]}{v_0^2 - v^2}}. \tag{2.28}$$

In fig. 2.3a we depict snapshots of the Huygens image wave, whereas in fig. 2.3b the construction of an image wavefront for a reflector migrated with a (possibly wrong) velocity is shown. For the sake of clarity, the figures are again reduced to two dimensions.

We now derive the eikonal equation in exactly the same way as we already did for the remigration in the depth domain in section 2.2: we substitute the eikonal $V(x,y,t)$ for the velocity v. Subsequently, we calculate the derivatives of the Huygens image wave (2.28) with respect to x, y and t. The sum of the squared derivatives with respect to x and y is

$$\begin{aligned} 0 &= \left(V_x^2 + V_y^2\right) \frac{16V^2\left[(x-x_0)^2 + (y-y_0)^2\right]^2}{\left(v_0^2 - V^2\right)^4 \left(t_0^2 + \frac{4\left[(x-x_0)^2+(y-y_0)^2\right]}{v_0^2-V^2}\right)} \\ &- \frac{16\left[(x-x_0)^2 + (y-y_0)^2\right]}{\left(t_0^2 + \frac{4\left[(x-x_0)^2+(y-y_0)^2\right]}{v_0^2-V^2}\right)\left(v_0^2 - V^2\right)^2}, \end{aligned} \tag{2.29}$$

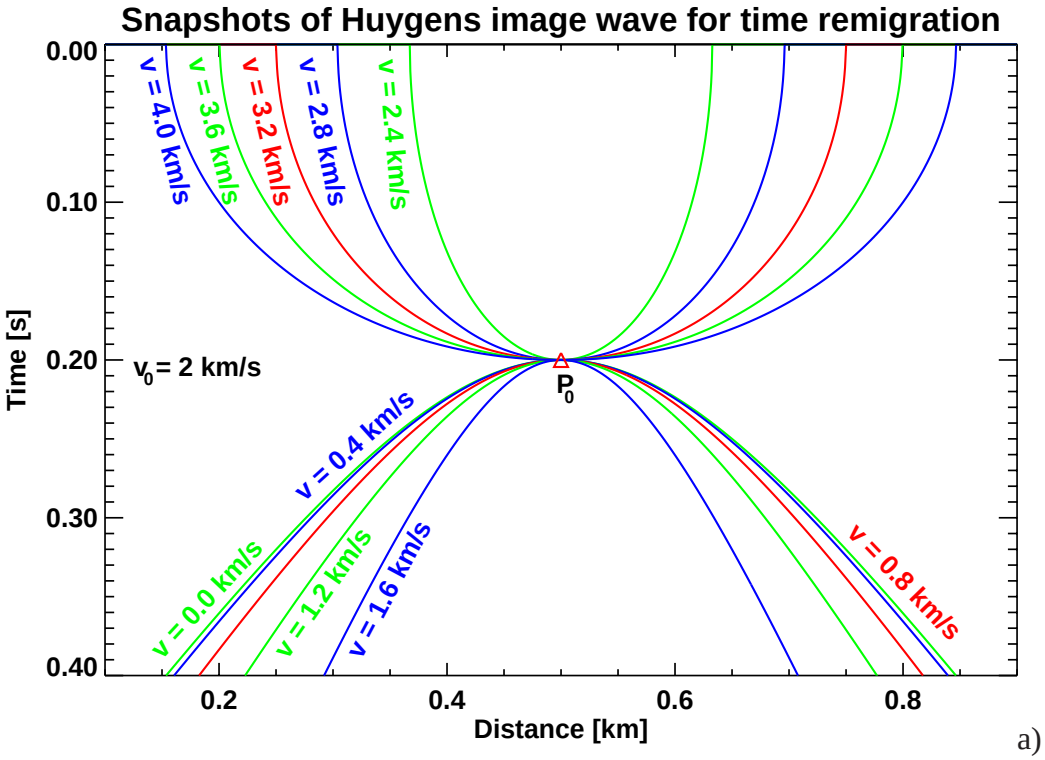

a)

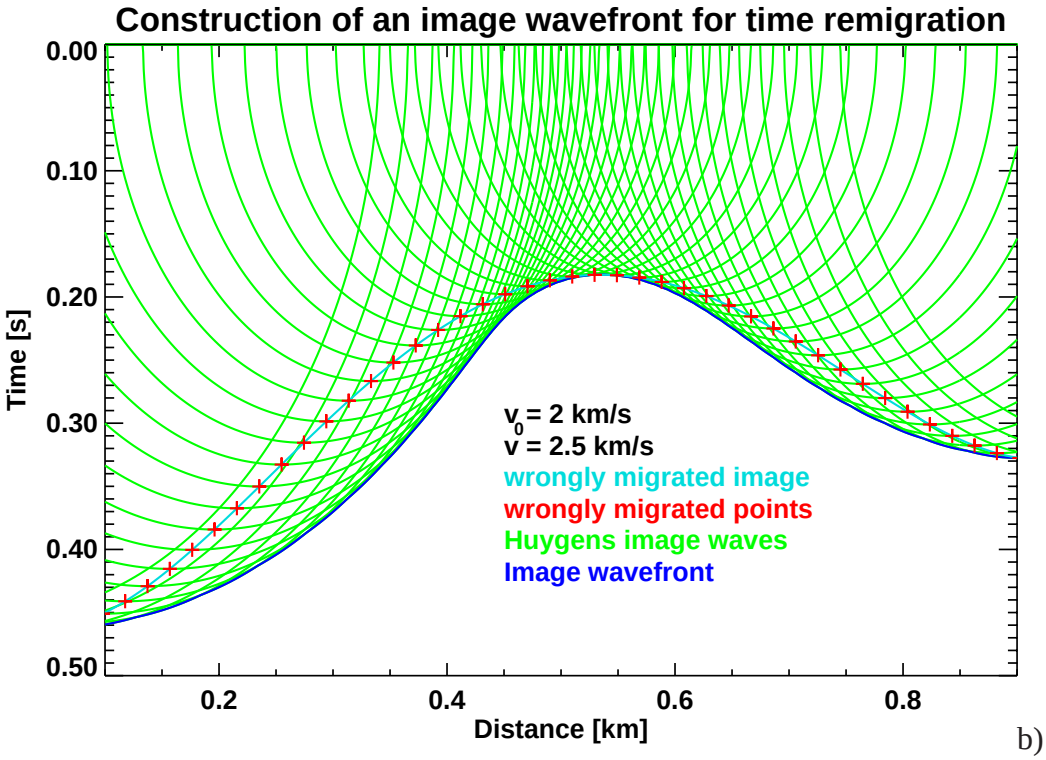

b)

Figure 2.3: a) Snapshots of a Huygens image wave in time domain for different velocities, b) construction of an image wavefront for the remigration in the time domain.

the derivative with respect to t, squared and divided by V_t^2 yields

$$\frac{1}{V_t^2} = \frac{16V^2\left[(x-x_0)^2+(y-y_0)^2\right]^2}{\left(v_0^2-V^2\right)^4\left(t_0^2+\frac{4\left[(x-x_0)^2+(y-y_0)^2\right]}{v_0^2-V^2}\right)}. \tag{2.30}$$

Inserting the equations (2.30) and (2.28) into equation (2.29) leads to

$$\frac{V_x^2+V_y^2}{V_t^2}\frac{t^2}{4} = 4\frac{(x-x_0)^2+(y-y_0)^2}{\left(v_0^2-V^2\right)^2}. \tag{2.31}$$

We insert this result (2.31) into the derivative with respect to t (2.30) and finally obtain the eikonal equation

$$V\left(V_x^2+V_y^2\right)-4V_t = V\left(\nabla V\right)^2-4\frac{\partial V}{\partial t} = 0. \tag{2.32}$$

Now, we again change to vector notation to get a more compact representation. We define $\nabla = (\partial/\partial x, \partial/\partial y)$.

As before for the remigration in the depth domain, the eikonal equation (2.32) gets equivalent to the corresponding equation by Hubral et al. [HTS96] if we reduce it to two dimensions. Following the image wave equation

$$vt\frac{\partial^2 p}{\partial x^2}+4\frac{\partial^2 p}{\partial v\partial t} = 0 \tag{2.33}$$

proposed in the cited paper for two dimensions, we propose a more general equation in 3D:

$$vt\nabla^2 p+4\frac{\partial^2 p}{\partial v\partial t} = 0 \tag{2.34}$$

Inserting the ansatz

$$p(x,y,t,v) = p_0(x,y,t)\,f\left[v-V(x,y,t)\right] \tag{2.35}$$

analogous to equation (2.1) into the proposed image wave equation (2.34) we obtain

$$f''p_0\left[vt\left(\nabla V\right)^2+4\frac{\partial V}{\partial t}\right]+f'\left(4\frac{\partial p_0}{\partial t}-2vt\nabla p_0\cdot\nabla V-vtp_0\nabla^2 V\right)+f\left(vt\nabla^2 p_0\right) = 0. \tag{2.36}$$

The expression in square brackets is equivalent to the eikonal equation (2.32) if we substitute the eikonal V for the velocity v. This indicates that the image wave equation (2.34) describes the kinematical properties of the remigration in the time domain. The corresponding initial value problem reads

$$p(v=v_0,x,y,t) \to p(v,x,y,t). \tag{2.37}$$

2.4 Migration to zero-offset (MZO)

For the derivation of the Huygens image waves for the two remigration problems we started with a point on a reflector in the initial data set. The resulting Huygens image waves emanate from this initial point and are, therefore, called exploding Huygens waves.

Now, we reverse this strategy for the migration to zero-offset: We consider the inverse problem, i. e. the migration to common-offset (MCO) and derive the Huygens image wave. This yields the exploding Huygens image wave for the inverse problem, which is equivalent to the imploding Huygens image wave for the original problem.

The inverse problem, i. e. the MCO, does not start with a migrated image but with the traveltimes. Therefore, we interchange the steps to derive the Huygens image wave: a point $P_0(\xi_0, t_0)$ in the zero-offset data set gets migrated into the depth domain. We obtain half-circles with radius $vt_0/2$ centered at $(\xi_0, 0)$ as isochrons:

$$z = \sqrt{\left(\frac{vt_0}{2}\right)^2 - (x-\xi_0)^2}\,. \tag{2.38}$$

Now, we demigrate each point $P(x,z)$ on the isochron (2.38) with the offset h. The common-offset traveltime curve for a point $P(x,z)$ reads

$$t = \frac{1}{v}\left[\sqrt{z^2 + (x-\xi+h)^2} + \sqrt{z^2 + (x-\xi-h)^2}\right]\,. \tag{2.39}$$

We obtain the family of traveltime curves for all points on the isochron by inserting the isochron equation into the traveltime curve (2.39):

$$t = \frac{1}{v}\left[\sqrt{\Psi^2 - (x-\xi_0)^2 + (x-\xi+h)^2} + \sqrt{\Psi^2 - (x-\xi_0)^2 + (x-\xi-h)^2}\right] \tag{2.40}$$

In this equation, $\Psi = vt_0/2$ denotes the length of the zero-offset ray path. The envelope of the family of traveltime curves (2.40) is defined by the condition $\partial t/\partial x = 0$. This leads to

$$\frac{\xi_0 - \xi + h}{\sqrt{\Psi^2 - (x-\xi_0)^2 + (x-\xi+h)^2}} + \frac{\xi_0 - \xi - h}{\sqrt{\Psi^2 - (x-\xi_0)^2 + (x-\xi-h)^2}} = 0\,, \tag{2.41}$$

subsequent solving for x yields

$$x = \frac{\xi_0^3 - \Psi^2\xi_0 + \Psi^2\xi - 2\xi_0^2\xi - \xi_0 h^2 + \xi_0\xi^2}{(\xi_0 - \xi - h)(\xi_0 - \xi + h)} = \xi_0 + \Psi^2\frac{\xi_0 - \xi}{h^2 - (\xi_0 - \xi)^2}\,. \tag{2.42}$$

Inserting equation (2.42) into the family of traveltime curves, we finally obtain the exploding Huygens image wave for the MCO problem. To avoid confusion, we firstly consider the arguments of the square roots in the equation of the family of traveltime curves (2.40):

$$\Theta_\pm = \Psi^2 - (x-\xi_0)^2 + (x-\xi\pm h)^2 \tag{2.43}$$

Substituting x according to equation (2.42) we obtain

$$\begin{aligned}\Theta_{\pm} &= \Psi^2 - \left(\Psi^2 \frac{\xi_0-\xi}{h^2-(\xi_0-\xi)^2}\right)^2 + \left(\xi_0-\xi \pm h + \Psi^2 \frac{\xi_0-\xi}{h^2-(\xi_0-\xi)^2}\right)^2 \\ &= \Psi^2 - \left(\frac{\Psi^2\Phi}{h^2-\Phi^2}\right)^2 + \left(\Phi \pm h + \frac{\Psi^2\Phi}{h^2-\Phi^2}\right)^2 \end{aligned} \tag{2.44}$$

with $\Phi = \xi_0 - \xi$. The family of traveltime curves (2.40), multiplied by v and squared now reads

$$\begin{aligned}(vt)^2 &= \left(\sqrt{\Theta_+}+\sqrt{\Theta_-}\right)^2 = \Theta_+ + \Theta_- + 2\sqrt{\Theta_+\Theta_-} \\ &= 2\frac{h^4+\Psi^2h^2-\Phi^4+\Psi^2\Phi^2}{h^2-\Phi^2} + 2\left(\Psi^2-\Phi^2+h^2\right) \\ &= 4h^2\frac{\Psi^2+h^2-\Phi^2}{h^2-\Phi^2} = 4h^2\left(1+\frac{\Psi^2}{h^2-\Phi^2}\right). \end{aligned} \tag{2.45}$$

After resubstituting $\Phi = \xi_0 - \xi$ we obtain the exploding Huygens image wave for the MCO problem

$$t = \frac{2h}{v}\sqrt{1+\frac{\Psi^2}{h^2-\Phi^2}} = \frac{2h}{v}\sqrt{1+\frac{\Psi^2}{h^2-(\xi_0-\xi)^2}} \tag{2.46}$$

which is equivalent to the imploding Huygens image wave for the MZO problem.

The construction of this Huygens image wave is shown in fig. 2.4a for one fixed offset h, snapshots of the Huygens image wave are shown in fig. 2.4b. In fig. 2.5 we depict the construction of an imploding MZO image wavefront (or exploding MCO wavefront, respectively) for one offset.

Proceeding in the same way as we did for the remigration, we substitute the eikonal $H(\xi,t)$ for the offset h and take the partial derivatives with respect to ξ and t. The derivative with respect to t reads

$$1 = \frac{2H_t}{v}\sqrt{1+\frac{\Psi^2}{H^2-\Phi^2}} - \frac{2\Psi^2H^2H_t}{v\sqrt{1+\frac{\Psi^2}{H^2-\Phi^2}}(H^2-\Phi^2)^2}. \tag{2.47}$$

Under consideration of $\Phi_\xi = -1$, we obtain the derivative with respect to ξ

$$0 = \frac{2H_\xi}{v}\sqrt{1+\frac{\Psi^2}{H^2-\Phi^2}} - \frac{2\Psi^2H^2H_\xi}{v\sqrt{1+\frac{\Psi^2}{H^2-\Phi^2}}\,(H^2-\Phi^2)^2} - \frac{2\Psi^2H\Phi}{v\sqrt{1+\frac{\Psi^2}{H^2-\Phi^2}}(H^2-\Phi^2)^2}. \tag{2.48}$$

Using $h = H(\xi,t)$ and inserting the equations $tv/2H = \sqrt{1+\Psi^2/(H^2-\Phi^2)}$ and $\Psi^2/[(tv/2H)^2-1] = H^2-\Phi^2$ derived from equation (2.46) into the derivative with respect to t (2.47), we obtain

$$\frac{1}{H_t} = \frac{t}{H} - \frac{4H^3\left[\left(\frac{tv}{2H}\right)^2-1\right]}{v^2t(H^2-\Phi^2)} \tag{2.49}$$

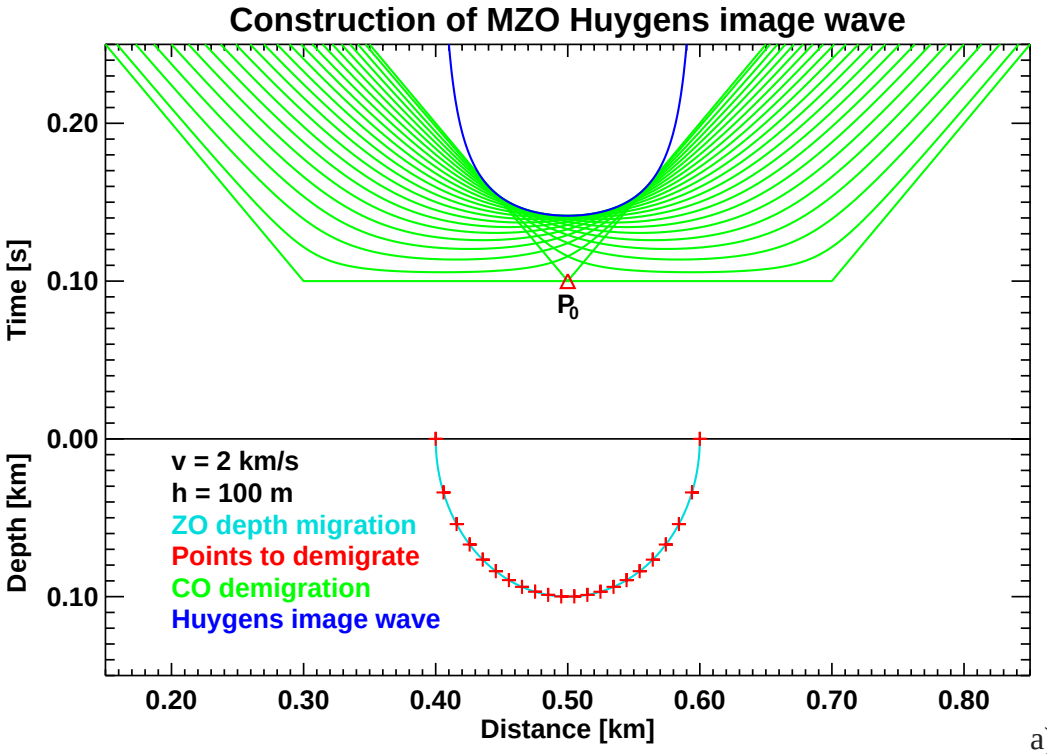

a)

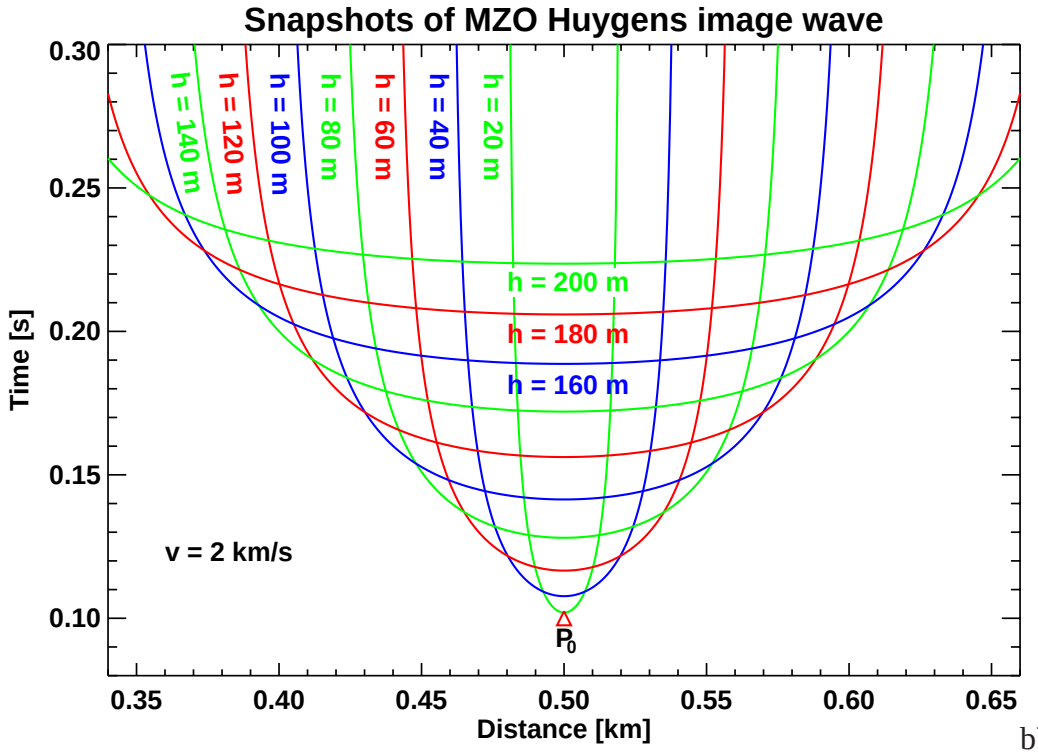

b)

Figure 2.4: a) Construction of the imploding Huygens image wave for the MZO problem, b) snapshot of the Huygens image wave for different offsets.

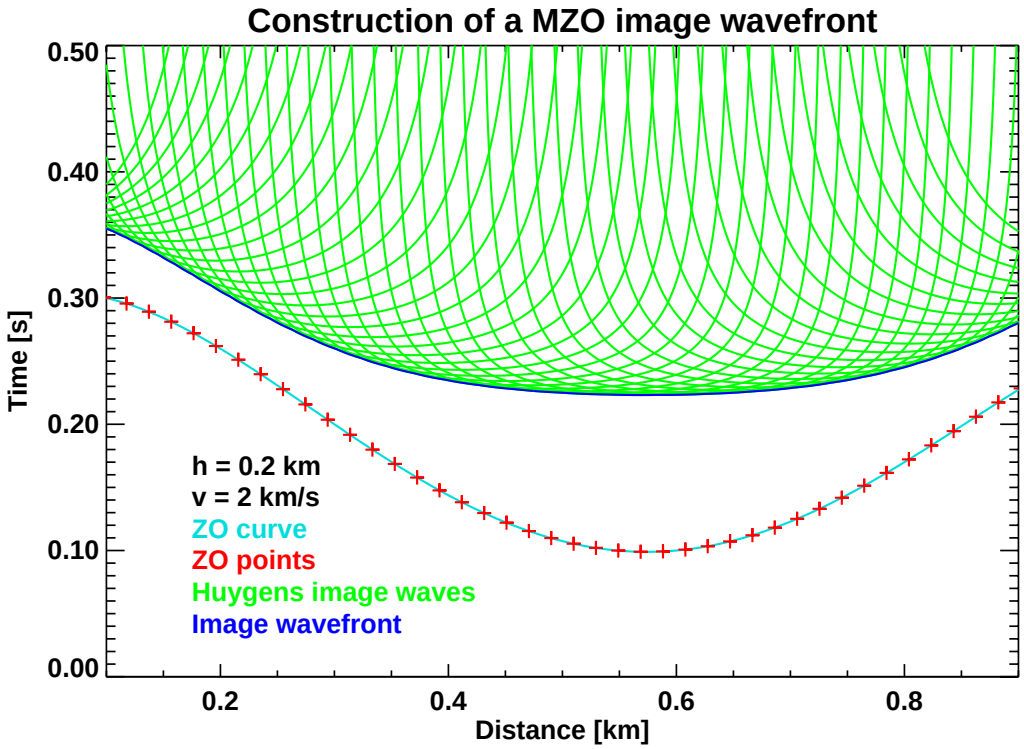

Figure 2.5: Construction of an MCO image wavefront for one offset.

and this leads to

$$H^2 - \Phi^2 = \frac{4H_t H^4 \left[\left(\frac{tv}{2H}\right)^2 - 1\right]}{v^2 t(H_t t - H)}. \tag{2.50}$$

The same procedure applied to the derivative with respect to ξ (2.48) yields

$$H_\xi = \frac{4H^3\Phi\left[\left(\frac{tv}{2H}\right)^2 - 1\right]}{t^2v^2(H^2 - \Phi^2) - 4H^4\left[\left(\frac{tv}{2H}\right)^2 - 1\right]}. \tag{2.51}$$

Inserting equation (2.50) into equation (2.51) leads to a simple expression for Φ

$$\Phi = \frac{H_\xi H^2}{tH_t - H} \tag{2.52}$$

which we insert into the equation (2.50). Finally, we obtain the eikonal equation for the MZO problem:

$$1 = H_\xi^2 - \frac{4H_t^2}{v^2} + \frac{tH_t}{H} + \frac{4HH_t}{v^2 t} \tag{2.53}$$

This eikonal equation is equivalent to the equation derived by Hubral et al. [HTS96][2]. In the same paper the image wave equation

$$ht\left(p_{hh} + \frac{4}{v^2}p_{tt}\right) + \left(t^2 + \frac{4h^2}{v^2}\right)p_{ht} - ht\,p_{\xi\xi} = 0 \tag{2.54}$$

[2]There is a factor 1/tB missing in equation (A28) of the cited paper

was proposed. Finally, we will show that we obtain the eikonal equation (2.53) if we insert an ansatz

$$p(\xi,t,h) = p_0(\xi,t)\, f[h - H(\xi,t)] \tag{2.55}$$

similar to equation (2.1):

$$\begin{aligned} 0 &= f'' p_0 \left[ht + \frac{4ht}{v^2} H_t^2 - \left(t^2 + \frac{4h^2}{v^2} \right) H_t - ht H_\xi^2 \right] \\ &- f' \left[\frac{8ht}{v^2} p_{0t} H_t + \frac{4ht}{v^2} p_0 H_{tt} - \left(t^2 + \frac{4h^2}{v^2} \right) p_{0t} - 2ht\, p_{0\xi} H_\xi + p_0 H_{\xi\xi} \right] \\ &+ f \left[\frac{4ht}{v^2} p_{0tt} - ht\, p_{0\xi\xi} \right] \end{aligned} \tag{2.56}$$

To satisfy equation (2.56) for any arbitrary function f, each term has to vanish separately. With $h = H(\xi,t)$ the term with f'' again leads to the derived eikonal equation (2.53). The image wave equation (2.54) obviously describes the kinematical aspects of the MZO problem. We are now able to rewrite the MZO problem as initial value problem:

$$p(h = h_0, \xi, t) \rightarrow p(h, \xi, t) \tag{2.57}$$

2.5 Dip moveout (DMO) correction

The MZO problem can be divided into two separate steps, i. e. the normal moveout (NMO) correction and the DMO. The NMO eliminates the influence of the offset for horizontal, non-dipping reflectors, whereas the DMO considers the dip of the reflectors.

To derive the eikonal equation for the DMO problem, we start with the exploding Huygens image wave for the MCO problem (2.46). Applying the well-known NMO correction (see e. g. Yilmaz [Yil87])

$$\tau^2 = t^2 - \frac{4h^2}{v^2} \tag{2.58}$$

to it, we obtain the Huygens image wave for the DMO problem:

$$\tau = \frac{t_0}{\sqrt{1 - \frac{\Phi^2}{h^2}}} \tag{2.59}$$

Snapshots of this imploding Huygens image wave are depicted in fig. 2.6a, the construction of an image wavefront for the inverse DMO problem is shown in fig. 2.6b.

Under consideration of $\partial\Phi/\partial\xi = -1$ we insert the eikonal $h = H(\xi,\tau)$ and obtain the derivatives with respect to ξ

$$0 = -t_0 \left(1 - \frac{\Phi^2}{H^2} \right)^{-\frac{3}{2}} \left(\frac{\Phi}{H^2} + \frac{\Phi^2 H_\xi}{H^3} \right) \tag{2.60}$$

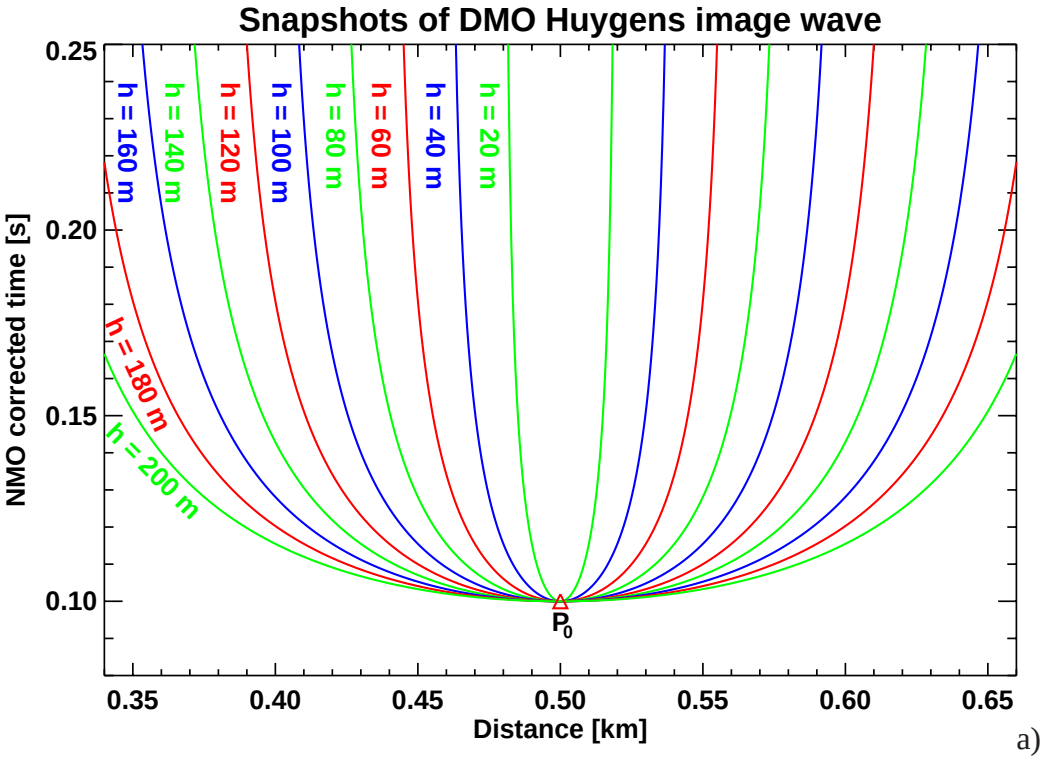

a)

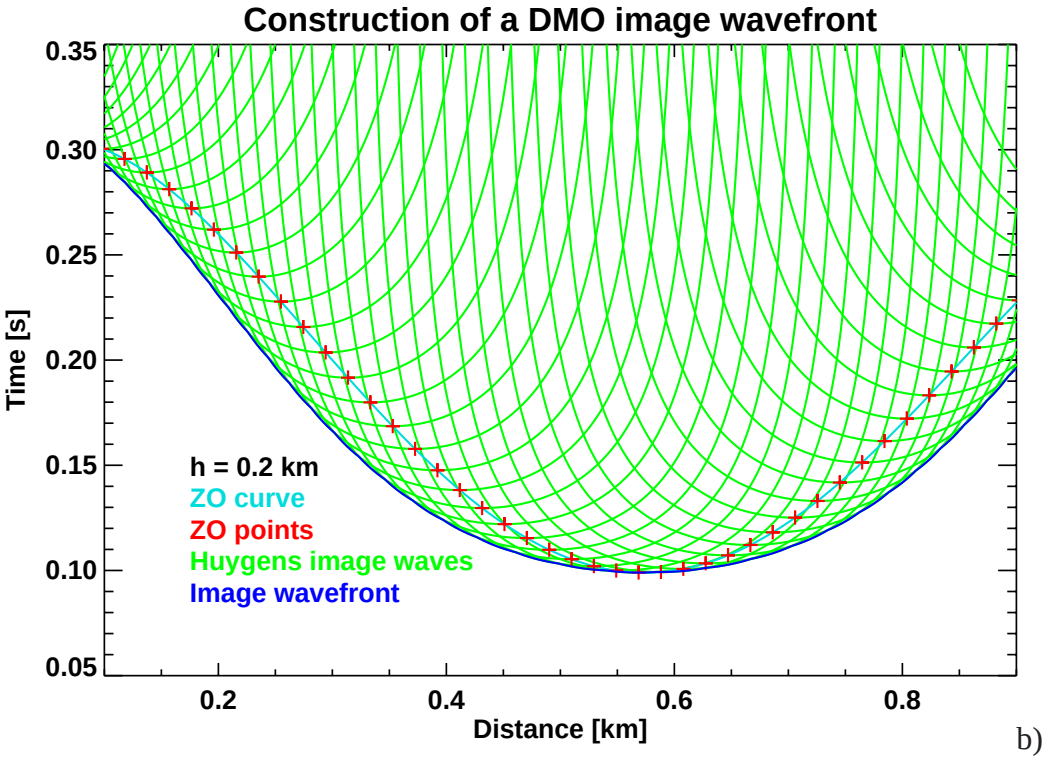

b)

Figure 2.6: a) Snapshots of the DMO Huygens image wave for different offsets, b) construction of an image wavefront for the inverse DMO problem.

and with respect to τ

$$1 = \frac{t_0 \Phi^2 H_\tau}{H^3} \left(1 - \frac{\Phi^2}{H^2}\right)^{-\frac{3}{2}} . \tag{2.61}$$

The derivative with respect to ξ (2.60) immediately leads to

$$\frac{1}{H_\xi} = -\frac{\Phi}{H} . \tag{2.62}$$

Using this equation (2.62) and the expression $t_0 = \tau\sqrt{1-\Phi^2/H^2}$ derived from the Huygens image wave (2.59) we obtain from the derivative with respect to τ (2.61)

$$H H_\xi^2 \left(1 - \frac{\Phi^2}{H^2}\right) = -\tau H_t , \tag{2.63}$$

and, by again inserting equation (2.62), the eikonal equation for the DMO problem:

$$-\tau H_\tau = H H_\xi^2 - H \tag{2.64}$$

This eikonal equation is equivalent to the equation derived by Hubral et al. [HTS96][3]. Finally, we have to show that the image wave equation

$$h p_{\xi\xi} - h p_{hh} - \tau p_{ht} = 0 \tag{2.65}$$

proposed in the cited paper leads to the derived eikonal equation if we use an ansatz

$$p(\xi, \tau, h) = p(\xi, \tau) f[h - H(\xi, \tau)] \tag{2.66}$$

similar to equation (2.1). With this ansatz we obtain

$$0 = f'' p_0 \left(h H_\xi^2 - h + \tau H_t\right) - f' \left(2 h p_{0\xi} H_\xi + h p_0 H_{\xi\xi} + \tau p_{0\tau}\right) + f p_{0\xi\xi} . \tag{2.67}$$

For an arbitrary function f this equations is only satisfied if the terms with f'', f' and f vanish separately. Using $h = H(\xi, \tau)$ the term with f'' again yields the eikonal equation (2.64). Therefore, the image wave equation (2.65) describes the kinematical properties of the DMO problem. The corresponding initial value problem reads

$$p(h = h_0, \xi, t) \to p(h, \xi, t) . \tag{2.68}$$

[3]The equations (29) and (A31) in the cited paper are incorrect: the square root on the right hand side should be in the denominator.

Chapter 3

Discretization and implementation

3.1 Remigration

3.1.1 Finite difference schemes

The finite difference (FD) schemes are derived from the image wave equations (2.23) and (2.34) which we repeat below to avoid confusion. In the depth domain we have

$$\nabla^2 p(x,y,z,v) + \frac{v}{z}\frac{\partial^2}{\partial z \partial v} p(x,y,z,v) = 0\,,$$

in the time domain

$$vt\nabla^2 p(x,y,t,v) + 4\frac{\partial^2}{\partial v \partial t} p(x,y,t,v) = 0\,.$$

These equations can be simplified by means of substitutions. In the depth domain the substitution $\rho = \ln v$ yields

$$\nabla^2 p^*(x,y,z,\rho) + \frac{1}{z}\frac{\partial^2}{\partial z \partial \rho} p^*(x,y,z,\rho) = 0\,, \tag{3.1}$$

and with $\omega = v^2$ we obtain for the time domain

$$t\nabla^2 p^*(x,y,t,\omega) + 8\frac{\partial^2}{\partial \omega \partial t} p^*(x,y,t,\omega) = 0\,. \tag{3.2}$$

With this substitutions both equations no longer explicitly depend on the velocity v, the propagation variables are the square or the logarithm of the velocity, respectively. These equations may be used instead of the original image wave equations.

Considering the four image wave equations (2.23), (2.34), (3.1) and (3.2), we now approximate the mixed derivatives by FD operators of first order according to equation (A.11),

second derivatives by FD operators of second order according to equation (A.5). Alternatively, we approximate second derivatives with respect to x and y by FD operators of fourth order according to equation (A.10). The FD operators are derived in the appendix A.

We have to distinguish the 2D and 3D problem, second order and fourth order operators as well as the time and depth domain. This leads to a total of 16 different FD schemes. To obtain a compact representation of all the schemes, we use the following conventions:

- The coordinates x, y and z are connected with the indices j, k and i, the respective fourth coordinate v, ω or ρ is connected with the index l. We name the related intervals of discretization Δx, Δy, Δz or Δt, respectively, and Δv, $\Delta\omega$ or $\Delta\rho$, respectively. We define $x = j\Delta x + x_0$ etc.
- In the depth domain, we use $\Xi = \Delta v/v$ in the case of "normal" velocity and $\Xi = \Delta\rho$ in the case of logarithmic velocity.
- In the time domain, we use $\Lambda = v\,\Delta v$ in the case of "normal" velocity and $\Lambda = \Delta\omega/2$ in the case of squared velocity.
- All expressions printed in green are to be omitted in the application to 2D data sets. In this case the index k has no meaning.

Using these conventions and solving for $p^{l+1}_{i,j,k}$ we obtain the following four equations, which describe the 16 implemented FD schemes for remigration problems:

Time domain, FD operators of max. second order:

$$\begin{aligned} p^{l+1}_{i,j,k} &= \frac{\Lambda t\,\Delta t}{4}\left[\frac{p^l_{i,j-1,k} - 2\,p^l_{i,j,k} + p^l_{i,j+1,k}}{\Delta x^2} + \frac{p^l_{i,j,k-1} - 2\,p^l_{i,j,k} + p^l_{i,j,k+1}}{\Delta y^2}\right] \\ &+ p^{l+1}_{i+1,j,k} - p^l_{i+1,j,k} + p^l_{i,j,k} \end{aligned} \tag{3.3}$$

Time domain, FD operators of max. fourth order:

$$\begin{aligned} p^{l+1}_{i,j,k} &= \frac{\Lambda t\,\Delta t}{48}\left[\frac{16\left(p^l_{i,j-1,k} + p^l_{i,j+1,k}\right) - p^l_{i,j-2,k} - p^l_{i,j+2,k} - 30\,p^l_{i,j,k}}{\Delta x^2}\right. \\ &+ \left.\frac{16\left(p^l_{i,j,k-1} + p^l_{i,j,k+1}\right) - p^l_{i,j,k-2} - p^l_{i,j,k+2} - 30\,p^l_{i,j,k}}{\Delta y^2}\right] \\ &+ p^{l+1}_{i+1,j,k} - p^l_{i+1,j,k} + p^l_{i,j,k} \end{aligned} \tag{3.4}$$

Depth domain, FD operators of max. second order:

$$p^{l+1}_{i,j,k} = \Xi z\,\Delta z\left[\frac{p^l_{i,j-1,k} - 2\,p^l_{i,j,k} + p^l_{i,j+1,k}}{\Delta x^2} + \frac{p^l_{i,j,k-1} - 2\,p^l_{i,j,k} + p^l_{i,j,k+1}}{\Delta y^2}\right.$$

$$+ \quad \frac{p^l_{i+1,j,k} - 2\,p^l_{i,j,k} + p^l_{i-1,j,k}}{\Delta z^2} \Bigg] + p^{l+1}_{i+1,j,k} - p^l_{i+1,j,k} + p^l_{i,j,k} \tag{3.5}$$

Depth domain, FD operators of max. fourth order:

$$\begin{aligned} p^{l+1}_{i,j,k} \;=\; & \Xi z \Delta z \left[\frac{16\left(p^l_{i,j-1,k} + p^l_{i,j+1,k}\right) - p^l_{i,j-2,k} - p^l_{i,j+2,k} - 30\,p^l_{i,j,k}}{12\Delta x^2} \right. \\ & + \frac{16\left(p^l_{i,j,k-1} + p^l_{i,j,k+1}\right) - p^l_{i,j,k-2} - p^l_{i,j,k+2} - 30\,p^l_{i,j,k}}{12\Delta y^2} \\ & + \left. \frac{p^l_{i+1,j,k} - 2\,p^l_{i,j,k} + p^l_{i-1,j,k}}{\Delta z^2} \right] + p^{l+1}_{i+1,j,k} - p^l_{i+1,j,k} + p^l_{i,j,k} \end{aligned} \tag{3.6}$$

Equation (3.3) was firstly introduced for two dimensions and squared velocity by Jaya et al. [JSH96][1]. For ”normal” velocity and in three dimensions it was introduced by Mann et al. [MJ97a].

Considering the FD schemes (3.3) – (3.6), we always find an expression $p^{l+1}_{i+1,j,k}$ on the right hand side. As the index l is related to the propagation variable, we are not able to determine the section p^{l+1} entirely from the preceding section p^l. That is why we call the FD schemes semi-explicit.

3.1.2 Implementation

In the beginning we intended to extend an existing program by Makky S. Jaya. However, numerous extensions and generalizations finally led to a completely new implementation of the remigration in the depth and time domain.

Whereas the FD schemes (3.3) – (3.6) are easy to implement without further ado, we have to consider the treatment of the edges of the computational space as well as the definition of the I/O formats and the parameter handling. Furthermore, the working direction for the calculation of the section p^l has to be determined. In the following we will discuss each of these items:

At the edges of the in general four-dimensional computational space we get in trouble with the boundary values because some of the values needed to calculate the FD operators are missing. We implemented two alternative solutions for this problem, an approximative solution and an exact solution:

For the approximative solution we proceed as follows: according to equation (A.10) five values are required to calculate the FD operators of fourth order. If not all five values are

[1] Equation (5) in the cited paper is obviously incorrect: there is a factor 2 missing in the denominator on the right hand side.

available, we apply FD operators of second order requiring only three values. One of these three values may still be missing. In this case we replace it by the value of its nearest neighbour. This artificial boundary condition is also called zero-slope condition and takes effect at the edges of the computational space for one or more of the FD operators. This method causes no considerable distortion in the numerical experiments.

The exact solution avoids this problems in the most straightforward way be successively shrinking the computational space in all directions. After each calculation step $p^l \rightarrow p^{l+1}$ we shrink the computational space in such a manner that all required values outside the shrunken space are available. Obviously, this method is only useful for a sufficiently big initial data volume, otherwise the target zone under investigation will be situated outside the remaining computational space. To obtain sections with an uniform geometry, regions outside the shrunken computational space are padded with zeros.

At the edges of the computational space values are also missing due to the fact that the FD schemes are semi-explicit. We tried to apply the mentioned zero-slope condition in this context, i. e. to replace the missing values in the section p^{l+1} by the corresponding values in section p^l (nearest neighbours in v-direction). Depending on the working direction (see below), these are the values of $p^{l+1}_{i_{\max},j,k}$ or $p^{l+1}_{0,j,k}$, respectively. Actually, we apply this condition only to the first velocity step. For the next steps, the condition—as well as some attempts to interpolate the missing values from their neighbours—leads to an unstable process. Presently, we have no satisfactory solution for this particular problem but simply keep the initial values. This may cause artifacts for the remigration in the depth domain. In the time domain, however, we obtain no artifacts due to this problem in the numerical experiments.

For parameter handling and data I/O we use libraries of the SEPlib package (Stanford Exploration Project). This enables us to implement the remigration in an almost hardware-independent way. Furthermore, the implementation can be used in connection with other SEPlib programs.

The working direction inside the computational space is of great importance for the stability of the FD method. Advancing to higher velocities, we have to start with the highest values of t or z, respectively, and vice versa. In the latter case the FD schemes (3.3) – (3.6) are solved for $p^{l+1}_{i,j,k}$.

The first implementation was written in Ratfor, but due to considerable problems with the pseudo-dynamical memory allocation it was rewritten in Fortran90. The new version is more compact and the code runs faster.

Essential features of the program:

- The input data set is an image in the time or depth domain migrated with a velocity v_0. In time domain it may also be a zero-offset section or a corresponding simulation (e. g. a CMP stack) related to the velocity $v_0 = 0$.
- The output data set has the geometry of the input data set plus the velocity as addi-

tional dimension. An arbitrary number of velocity steps may be chosen independently for the actual calculation and the output.[2]

- The propagation variable may be chosen as "normal" velocity, squared velocity (time domain), or logarithmic velocity (depth domain).
- We can define an arbitrary target zone within the initial data set.
- Partial derivatives with respect to x and y can be approximated by FD operators of either second or fourth order. [3]

3.2 Normal moveout (NMO), DMO and MZO

3.2.1 Finite difference schemes

The derivation of the FD schemes is directly based on the derived image wave equations for the MZO (2.54) and DMO (2.65) problems. For the MZO problem we have

$$ht\left(p_{hh}+\frac{4}{v^2}p_{tt}\right)+\left(t^2+\frac{4h^2}{v^2}\right)p_{ht}-ht\,p_{\xi\xi}=0$$

and for the DMO problem

$$hp_{\xi\xi}-hp_{hh}-\tau p_{ht}=0\,.$$

Once again we approximate the mixed derivatives by FD operators according to equation (A.11). Second order derivatives with respect to h and t are approximated by FD operators of second order according to equation (A.5), second derivatives with respect to ξ by FD operators of fourth order according to equation (A.10).

We use the following conventions for the FD schemes:

- The coordinates ξ and t or τ, respectively, are connected with the indices j and i, the coordinate h is connected with the index l. We name the corresponding discretization intervals $\Delta\xi$ and Δt or $\Delta\tau$, respectively, defining $\xi = j\Delta\xi+\xi_0$ etc.
- For the MZO problem we abbreviate:

$$\Upsilon = t^2+\left(\frac{2h}{v}\right)^2 \tag{3.7}$$

[2]Restriction: for the remigration towards smaller velocities $v>0$ (depth domain) or $v\geq 0$ (time domain), respectively, must be satisfied.

[3]The new Fortran90 implementation always uses FD operators of fourth order.

Using all substitutions and conventions, we solve for $p_{i,j}^{l+1}$ and obtain the following two FD schemes:

Migration to zero-offset:

$$\begin{aligned} p_{i,j}^{l+1} &= \frac{1}{\Delta h \Upsilon - ht\Delta t}\left[ht\Delta t\left(p_{i,j}^{l-1} - 2\,p_{i,j}^{l}\right) + \frac{4\,ht\,\Delta h^2}{v^2\,\Delta t}\right. \\ &\times \left(p_{i+1,j}^{l} - 2p_{i,j}^{l} + p_{i-1,j}^{l}\right) + \Upsilon\Delta h\left(p_{i+1,j}^{l+1} - p_{i+1,j}^{l} + p_{i,j}^{l}\right) \\ &- \left.\frac{ht\Delta h^2\Delta t}{12\Delta\xi^2}\left(16\left\{p_{i,j-1}^{l} + p_{i,j+1}^{l}\right\} - p_{i,j-2}^{l} - p_{i,j+2}^{l} - 30\,p_{i,j}^{l}\right)\right] \end{aligned} \tag{3.8}$$

Dip moveout correction:

$$\begin{aligned} p_{i,j}^{l+1} &= \left[\frac{h\Delta h^2\Delta\tau}{12\Delta\xi^2}\left(16\left\{p_{i,j-1}^{l} + p_{i,j+1}^{l}\right\} - p_{i,j-2}^{l} - p_{i,j+2}^{l} - 30p_{i,j}^{l}\right)\right. \\ &- \left.h\Delta\tau\left(p_{i,j}^{l-1} - 2p_{i,j}^{l}\right) - \tau\Delta h\left(p_{i+1,j}^{l+1} - p_{i+1,j}^{l} + p_{i,j}^{l}\right)\right]\frac{1}{h\Delta\tau - \tau\Delta h} \end{aligned} \tag{3.9}$$

Similar to the FD schemes for remigration in section 3.1.1, the FD schemes (3.8) and (3.9) are semi-explicit: we have the term $p_{i+1,j}^{l+1}$ on the right hand side in both cases. The section p^{l+1} is not entirely determined by the preceding section p^{l}.

3.2.2 Implementation of the NMO correction

Although the NMO correction is not part of the DMO problem, it is included in the implementation. This enables us to compare the results of the MZO and the NMO/DMO without using any additional software.

Another reason to include the NMO is the fact that most of the available NMO programs expect common-shot gathers. With the included NMO there is no need to transform the data sets from the common-shot to the common-offset configuration.

To apply the mentioned NMO correction (2.58)

$$\tau^2 = t^2 - \frac{4h^2}{v^2}$$

we proceed as follows:

We preserve the geometry of the initial, not yet NMO corrected data set, i. e. the ranges of the corrected traveltime τ and the uncorrected traveltime t are the same. Firstly we calculate the subrange for τ for which data are available. Then, we determine the traveltime t_i for each sample τ_i in this subrange of the τ-domain. We perform a linear interpolation of the two samples around t_i and assign the result to the corrected traveltime τ_i. Areas without available data are padded with zeros.

Furthermore, we implemented two additional features:

The NMO correction causes a pulse stretch along the traces. The larger the offset h and the smaller the traveltimes τ, the larger the pulse stretch. This pulse stretch debases the result of a subsequent stacking procedure. Therefore, we implemented a routine to mute areas with a too large pulse stretch.

Providing the length of the wavelet t_w in the initial data set, we calculate the uncorrected travel time t_i for each corrected traveltime τ_i by means of equation (2.58). Afterwards, we compute $t_i + t_w$ and the corresponding corrected traveltime $\tau^*(t_i + t_w)$. To confine the pulse stretch to a maximum of 25%, we mute all samples satisfying $(\tau^* - \tau_i)/t_w > 1.25$.

With increasing offset the raypaths and the traveltime proportional to them (remember $v = const$) also increase. The difference between zero-offset and common-offset raypath causes an additional loss of amplitude called geometrical spreading. This effect can be easily set off by multiplying each sample by $\sqrt{t_i/\tau_i}$ (line source in 2D) or t_i/τ_i (point source in 3D), respectively. This so-called geometrical spreading correction is singular for $\tau \to 0$. Therefore, we confine it to an explicitly given maximum. Using the muting routine and geometrical spreading correction together will, however, never yield any singularities at all.

3.2.3 Implementation of the DMO and MZO

The situation is quite the same as for the remigration problems in section 3.1.2. Almost all statements made there also apply to the DMO and MZO problems. Once again we apply the zero-slope condition at the edges of the in this case three-dimensional computational space. For the first offset step we set the initial condition $p^0 \equiv p^1$, i. e. we apply the zero-slope condition to the offset-direction, too. A successive shrinking of the computational space as implemented for the remigration is not included.

The remigration is implemented towards higher as well as lower velocities, whereas the DMO and MZO is implemented for a propagation towards smaller offsets only. We define the offset interval Δh in such a manner that we obtain the desired number of offset steps for the largest offset in the initial data set. For smaller offsets h_i commensurate fewer offset steps are computed with the same offset interval Δh. To preserve an uniform geometry for output, we pad with zeros for $h_{\max} \geq h > h_i$ if necessary. This enables us to perform the stacking of the results easily. The propagation always terminates at $h \approx 0$.

The working direction is clearly determined by the direction of propagation $\Delta h < 0$: the FD schemes are stable only if we proceed from higher towards lower traveltimes t or τ, respectively. The sign of Δh also defines which values have to be provided again in each offset step due to the semi-explicit properties of the FD schemes (3.8) and (3.9): the values $p^{l+1}_{i_{\max},j}$ cannot be computed from the preceding section. In the present implementation these values are once set to $p^0_{i_{\max},j}$ and remain unchanged during the propagation process.

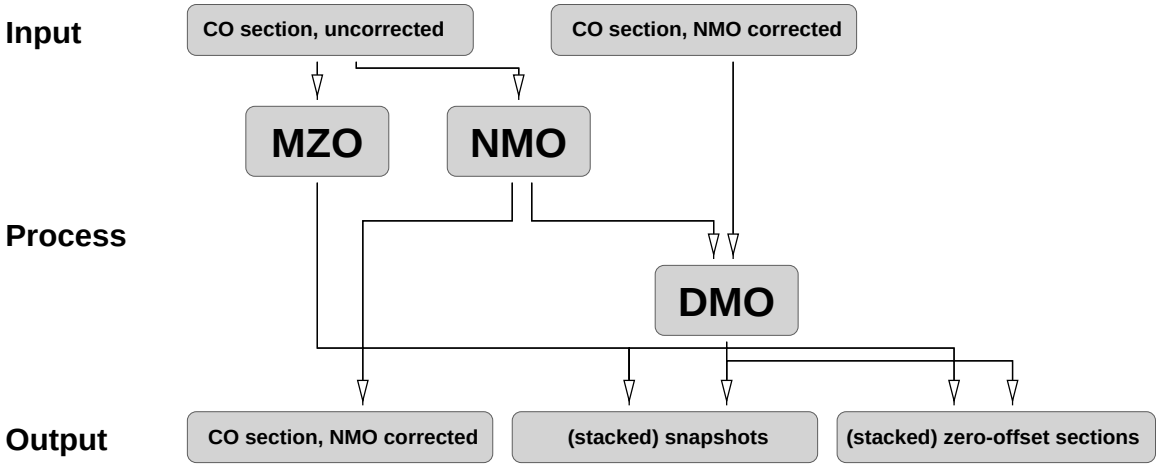

Figure 3.1: Possible applications of the NMO/DMO/MZO program.

The approximations mentioned above do not exercise an significant influence on the results of the numerical experiments. Whereas the DMO correction proved very stable, the unmodified MZO process fails: the MZO process is unstable with all parameter sets we considered so far. We obtain highest frequency artifacts with quickly increasing amplitudes covering any useful information. To force the MZO process to be stable, we propose an additional smoothing operator to be applied after each offset step. The operator is explained in appendix B. Its influence on the stability of the process and the resulting traveltimes is discussed in section 5.2.

The NMO/DMO/MZO implementation is written in Fortran90. As for the remigration we use programs of the SEPlib package to perform the data I/O and the parameter handling. The individual processes NMO, DMO and MZO may be applied separately or combined (NMO/DMO). The possible applications are depicted in fig. 3.1. As we implemented several ways of stacking, the program supports various I/O formats:

- Input:
  - an arbitrary number of uncorrected common-offset gathers $p(t,\xi)$
  - an arbitrary number of NMO-corrected common-offset gathers $p(\tau,\xi)$
- Output:
  - NMO-corrected common-offset gathers $p(\tau,\xi)$
  - Pre-stack snapshots of the MZO process $p(t,\xi,h,h_0)$. Here and in the following, h denotes the propagation variable in offset direction, whereas h_0 denotes the offset of the initial common-offset section.
  - Post-stack snapshots of the MZO process $p(t,\xi,h)$ stacked for identical offsets h.
  - Pre-stack zero-offset sections $p(t,\xi,h=0,h_0)$

- Post-stack zero-offset section $p(t,\xi,h=0)$
- Pre-stack snapshots of the DMO process $p(\tau,\xi,h,h_0)$
- Post-stack snapshots of the DMO process $p(\tau,\xi,h)$
- Pre-stack zero-offset sections $p(\tau,\xi,h=0,h_0)$
- Post-stack zero-offset section $p(\tau,\xi,h=0)$

Additional features of the program:

- We preserve the geometry of the initial data set. Depending on the chosen output format, we obtain an additional offset dimension with an user-defined number of offset steps. The number of offset steps for the actual calculation may be chosen independently.
- The NMO correction includes a geometrical spreading correction for a line or point source, respectively. The correction is limited to an explicitly given maximum.
- Areas with a pulse stretch larger than 25% can be muted during the NMO process. This requires the length of the wavelet.
- The stability of the MZO process is controlled by means of a smoothing parameter.

Chapter 4

Application of the remigration

4.1 Synthetic 2D data set

For testing purposes and to compare the remigration results with various migration methods, we define a 2D model satisfying the constant velocity assumption made during the derivation of the image wave equations: the model shown in fig. 4.1 consists of five layers with different densities but the same propagation velocity. We tried to chose a geologically reasonable model.

By means of exploding reflector modeling we simulate a zero-offset data set for this model. The result is shown in fig. 4.2a. The data set has a sampling rate of 1.3 ms and includes 120 traces with 50 m spacing. The mean frequency of the chosen wavelet is 30 Hz. The model and the related zero-offset data set was already used by Jaya et al. [JSH96]. Therefore, we are immediately able to compare the results of the original implementation and the one proposed in this thesis.

Not all reflectors are well illuminated due to the chosen zero-offset configuration, in particular strong dipping reflector segments are affected. As there is no information about non-illuminated reflector segments in the data set, they cannot be imaged by any imaging method at all.

In the following, we apply the remigration in the time and depth domain to this data set. In the time domain we can immediately use the zero-offset data set, in depth domain, however, we first have to generate a (conventionally) depth-migrated image.

4.1.1 Remigration in the time domain

We remigrate the synthetic data set in the time domain with 2000 velocity steps from $v = 0$ km/s to $v = 6$ km/s using “normal” velocity and FD operators of max. fourth order.

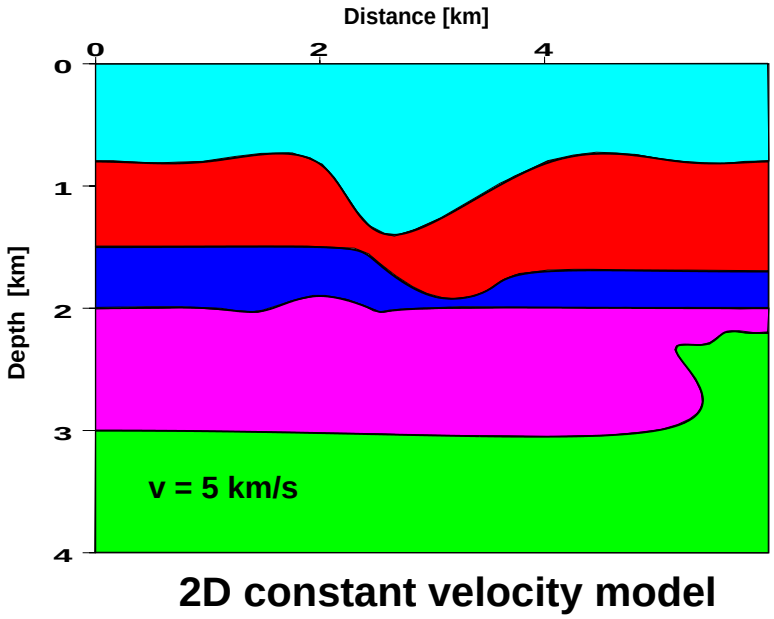

Figure 4.1: Two dimensional model with density contrasts and $v = 5$ km/s.

Comparing this result with the results calculated with FD operators of max. second order and/or squared velocity yields no significant differences and will not be discussed further. Only the stability of the process is slightly higher with squared velocity, i. e. we can use somewhat larger propagation steps $\Delta\omega$.

The last section of the mentioned remigration result[1], i. e. the result for $v = 6$ km/s, is taken as time-migrated image. We remigrate this image in a second process from $v = 6$ km/s down to $v = 0$ km/s using the same parameters as in the first process, merely the sign of Δv and the initial velocity v_0 are changed accordingly.

Now, we discuss the properties of the two remigration results:

First of all we consider the intrinsic consistency of the remigration method. For that purpose we extract the section related to $v = 0$ km/s from the second remigration result, i. e. the one calculated towards smaller velocities. This so-called pseudo zero-offset section should be—at least kinematically—equivalent to the initial zero-offset section. Both sections are shown in fig. 4.2. Leaving artifacts due to grid dispersion and influences of the edges out of account, the two sections are indeed equivalent.

Now, we extract the section for the true model velocity $v = 5$ km/s from the first remigration result ($\Delta v > 0$) and compare it with the results of several migration methods. In fig. 4.3 we have the results of the remigration, of a phase shift migration, of a migration in the t-k-domain, and finally of a Kirchhoff migration in the time domain for the model velocity $v = 5$ km/s. With respect to the kinematical properties the results are essentially equivalent.

[1] We omit the first and the last trace as well as the first and last time sample. This reduces the influences of artifacts at the edges.

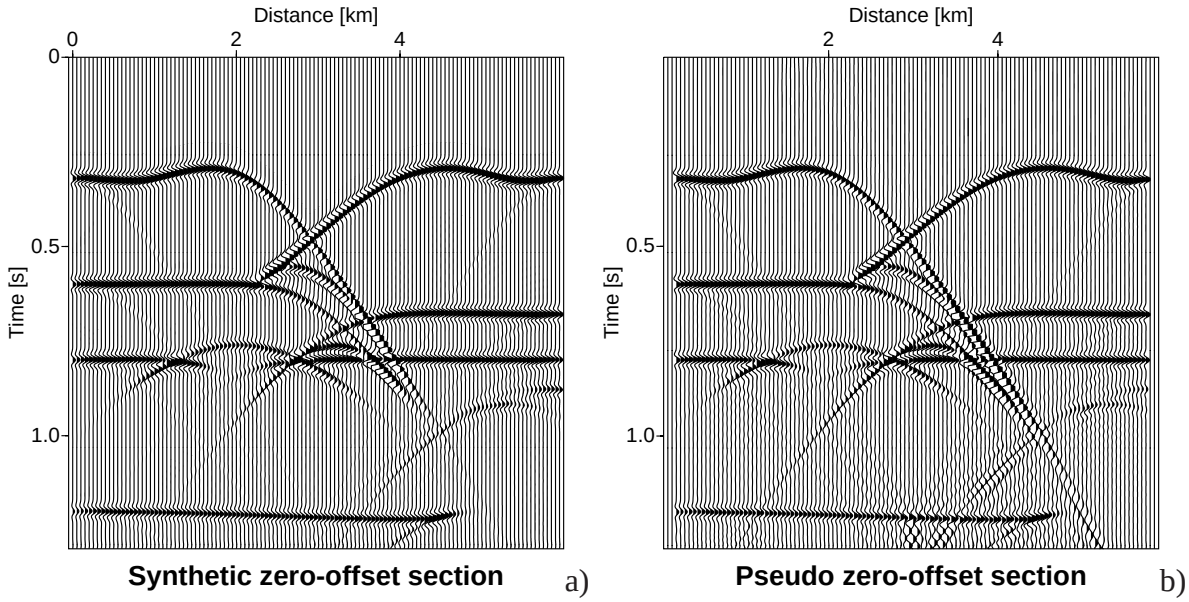

Figure 4.2: Synthetic 2D data set: a) zero-offset section, b) pseudo zero-offset section generated by remigrating twice.

Each method causes some specific artifacts: e. g. we get strong dispersion effects with the remigration in the vicinity of steep flanks, whereas the two migration methods working with discrete Fourier transformations (phase shift migration and migration in the t-k-domain) generate aliasing effects.

Finally, we show snapshots of the remigration process with $\Delta v > 0$ in fig. 4.4. With this representation we can observe the continuous changes, i. e. the propagation of the imaged reflectors with increasing velocity.

Of particular interest are the triplications mainly caused by the first reflector. These triplications vanish with increasing velocity. Disregarding the non-illuminated areas, we obtain continuous and correctly located images of the reflectors for the the true model velocity. For velocities higher than the true model velocity we observe hyperbolas well-known as smiles indicating a too high migration velocity.

Diffraction patterns and triplications turn out to be good indicators for the quality of the generated image. By observing such structures in the remigrated sections we can estimate an optimum constant migration velocity: for the true model velocity triplications should vanish and diffraction patterns should collapse to points. Obviously, the latter effect will not occur exactly in the numerical experiment, but actually the diffraction hyperbolas shrink to small flat objects.

The frequency content of the time-remigrated sections does not significantly depend on the instantaneous remigration velocity. As we will see for the remigration in the depth domain later on, this appears to be the crucial point for the stability of the remigration in the time domain towards *both* possible directions of propagation. According to fig. 4.2 the

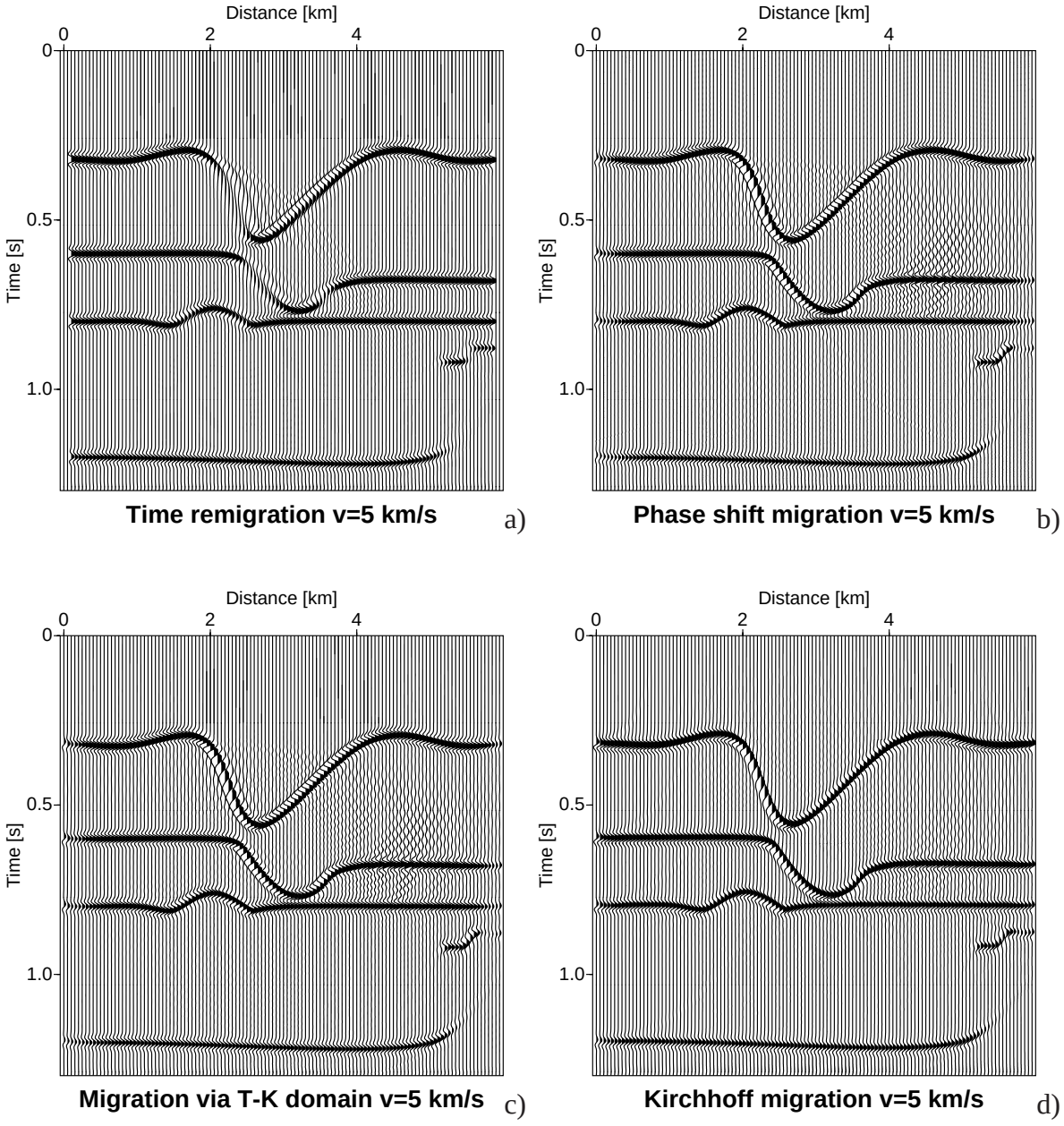

Figure 4.3: Synthetic 2D data set: results for $v = 5$ km/s computed by a) remigration in the time domain, b) phase shift migration, c) migration in the t-k-domain, d) Kirchhoff migration in the time domain.

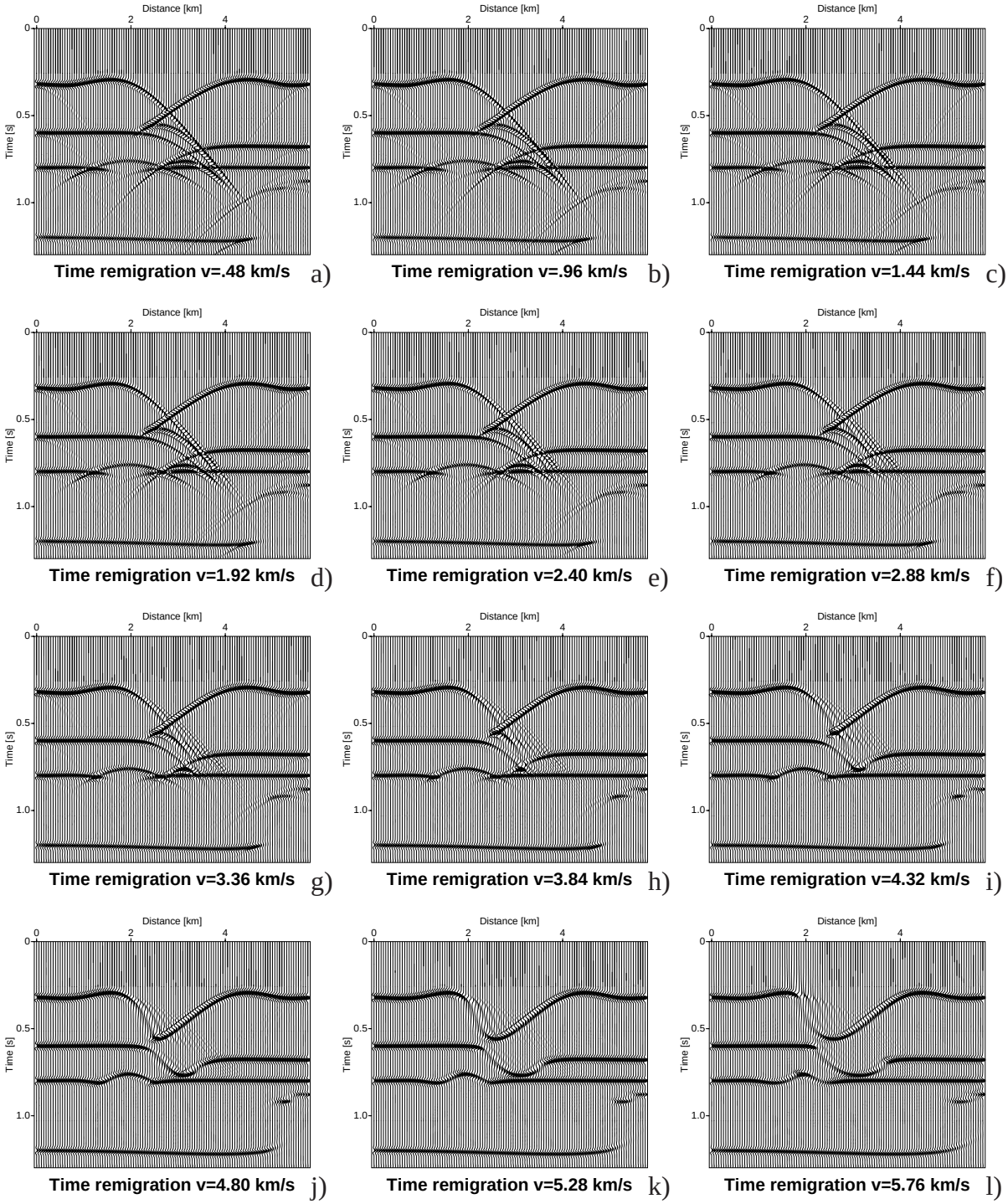

Figure 4.4: Synthetic 2D data set: time-remigrated sections for $v =$ a) 480, b) 960, c) 1440, d) 1920, e) 2400, f) 2880, g) 3360, h) 3840, i) 4320, j) 4800, k) 5280 and l) 5760 m/s.

remigration is obviously stable in both cases.

Finally, we will compare the computational costs: computing one of the (conventional) migration results in fig. 4.3 takes about the same processing time as the calculation of the 2000 remigration steps. For the discussed data set 25 of this steps are saved to disk, 12 of them are shown in fig. 4.4.

4.1.2 Remigration in the depth domain

We applied a phase shift migration with the wrong velocity $v = 4$ km/s to the zero-offset section shown in fig. 4.2a. The result is transformed from the time to the depth domain according to equation (2.27). Besides, we cut off some numerical artifacts at the lower edge of the migrated image.

As previously mentioned in section 3.1.2 the semi-explicit properties of the FD schemes (3.3) – (3.6) cause problems at the—depending on the direction of propagation—upper or lower edge of the computational space, respectively. In the depth domain we expect a mainly vertical propagation of the images so that images may propagate to the crucial upper or lower edge of the computational space, respectively. This causes considerable artifacts which, however, vanish again in the advancing process and do not significantly change the stability.

To avoid such artifacts, we padded the depth-migrated image with zeros in such a manner that the computational space is large enough to include all events for all velocities under consideration.

The depth-migrated image prepared in the discussed way is shown in fig. 4.5a. We applied a remigration in the depth domain in 2000 velocity steps from $v = 4$ km/s to $v = 6$ km/s using ”normal” velocity and FD operators of max. fourth order[2]. The resulting section for the true model velocity is shown in fig. 4.5b, further snapshots of the remigration process are shown in fig. 4.6.

By means of the underlying model in fig. 4.5b we can easily observe that the illuminated segments of the reflectors are correctly imaged with respect to their kinematical properties. As for the remigration in the time domain we obtain artifacts due to grid dispersion in the vicinity of steep flanks.

Having a close look at the snapshots in fig. 4.6 we observe that the wavelet is stretched with increasing velocity. This well-known pulse stretch also occurs for conventional migration methods and strongly controls the stability of the proposed FD methods: if we apply a remigration in the depth domain towards lower velocities, the frequency of the wavelet as well as of the unavoidable noise in the data set increases. As the highest representable frequency is given by the discretization intervals this normally leads to the instability of

[2]As for the remigration in the time domain we get no significant differences if we use FD operators of max. second order and/or—in this case—logarithmic velocity.

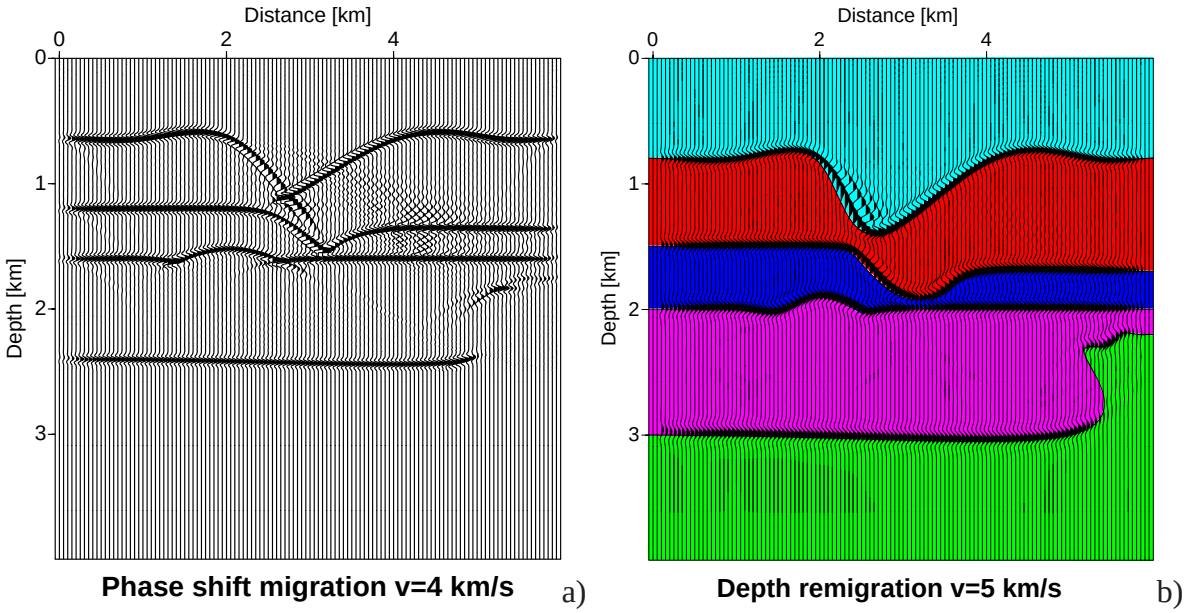

Figure 4.5: Synthetic 2D data set: a) result of a phase shift migration with $v = 4$ km/s, transformed to the depth domain, b) result of the remigration in the depth domain for $v = 5$ km/s with underlying model.

the process. According to the numerical experiments high frequency noise soon covers any useful information: the amplitudes quickly increase, the sign changes from sample to sample. This happens when the velocity decreases more than max. about 10%.

If the initial data set already contains some noise or high frequency artifacts, the remigration towards lower velocities totally fails. In fig. 4.7 we have an example for the instability: remigration is applied to the result of a phase shift migration with $v = 5.2$ km/s. We perform 400 velocity steps spaced 0.125 m/s and obtain only noise after a few calculation steps.

The required processing time is about the same as for the remigration in the time domain. Criteria for the image quality are once again vanishing triplications, collapsing diffraction hyperbolas and the continuity of the imaged reflectors.

4.2 Marmousi 3D overthrust model

In section 4.1 we used a synthetic data set which exactly satisfies the assumed homogeneous model. Now we explore what happens if we apply the remigration to inhomogeneous models using synthetic but very complex data sets generated for the Marmousi 3D overthrust model. This model shown in fig. 4.8 was developed at the Institut Français du Pétrole and at the Netherlands Institute of Applied Geoscience TNO by means of GOCAD.

The model includes considerable vertical and lateral inhomogeneities. The velocity varies between 2.2 and 6 km/s. The assumption of homogeneity is considerably offended.

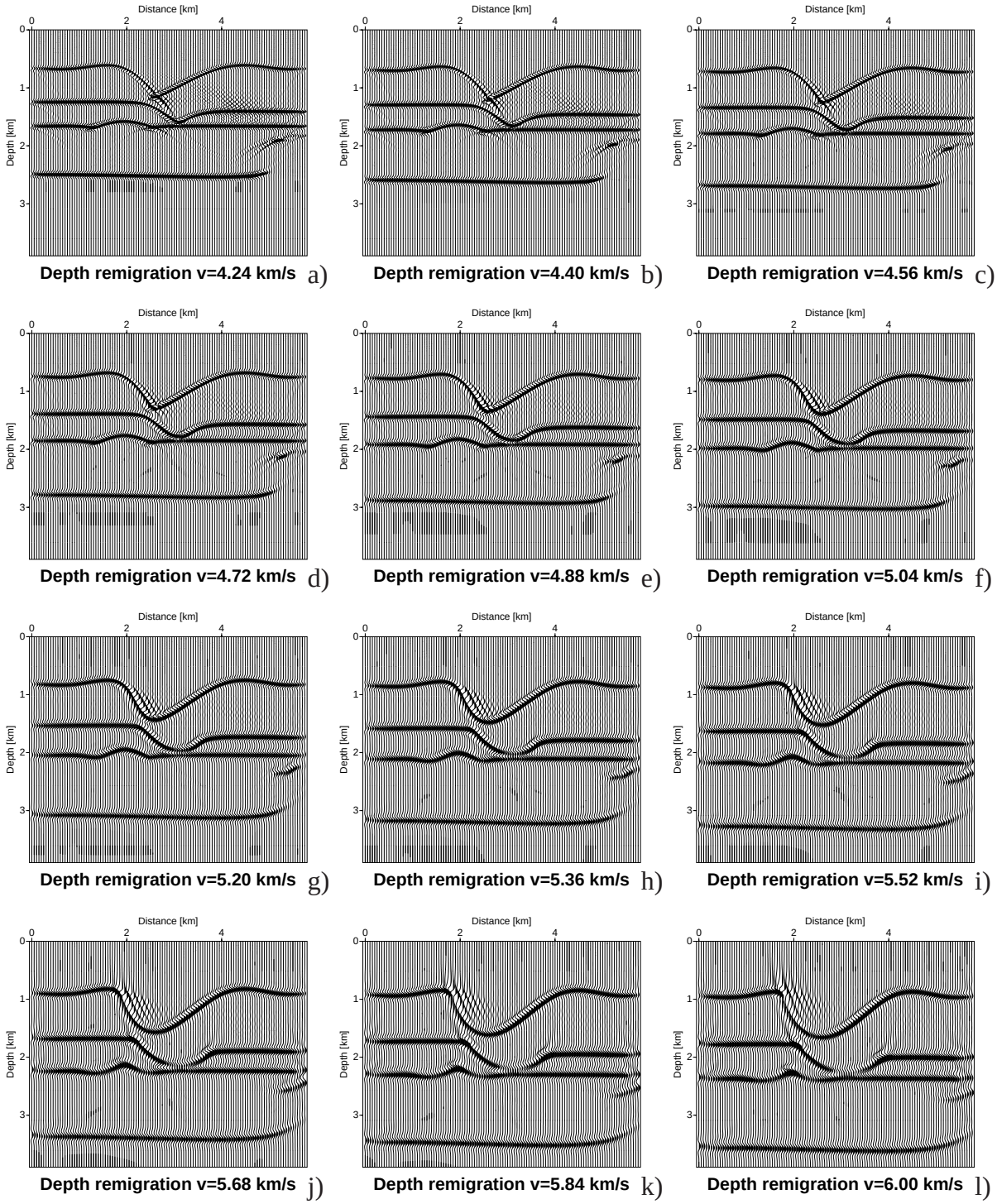

Figure 4.6: Synthetic 2D data set: depth-remigrated section for $v =$ a) 4240, b) 4400, c) 4560, d) 4720, e) 4880, f) 5040, g) 5200, h) 5360, i) 5520, j) 5680, k) 5840 and l) 6000 m/s.

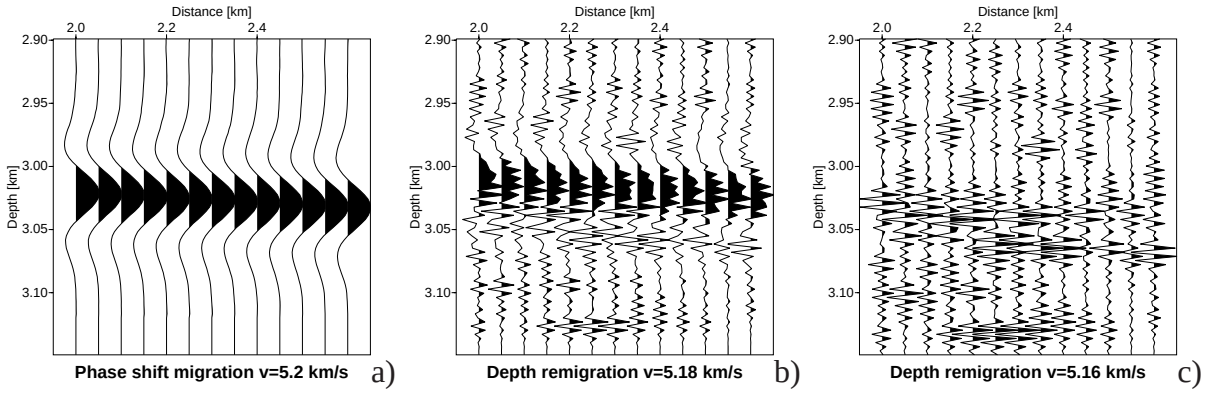

Figure 4.7: Synthetic 2D data set: a) detail of a phase shift migration result for $v = 5.2$ km/s, transformed to depth domain. Details of depth-remigrated sections for b) 5.18 and c) 5.16 km/s.

For the Marmousi 3D overthrust model a data set with a non-regular arrangement of zero-offset and near-offset traces is available. All traces consist of 350 samples with a sampling rate of 8 ms. As the remigration programme expects the data on a regular grid we have to prepare the data set accordingly:

In a first step we eliminated all near-offset traces. To get an idea of the geometry of the remaining zero-offset traces we depict their locations in fig. 4.9. Obviously, there are three regions for which we can extract data sets with regular geometries:

- A profile line oriented from east to west with 312 traces spaced 50 m. We call this data set the 2D data set.[3]
- A 3D data set with 18 profile lines oriented from east to west in a distance of 600 m. Each line contains 151 traces spaced 100 m. We call this data set the asymmetric 3D data set.
- A 3D data set with 11 profile lines oriented from east to west in a distance of 100 m. Each line contains 101 traces spaced 100 m. This data set is called the symmetric 3D data set.

Although it is a synthetic data set some traces are missing in the three chosen data subsets. Furthermore, some of the traces turn out to be useless. We replace these useless and missing traces by zero traces. In a next step we replace the empty traces by neighbouring traces or—if possible—by linear interpolations of the neighbouring traces. In this way finally all three data subsets are entirely filled with usable traces.

We apply the remigration in the time domain to the three extracted data subsets. A preceding (conventional) migration is not necessary in this case. As migrated images in the depth

[3]This data set was computed for the 3D model and is therefore not equivalent to a data set which we would obtain for the 2D model in fig. 4.8b.

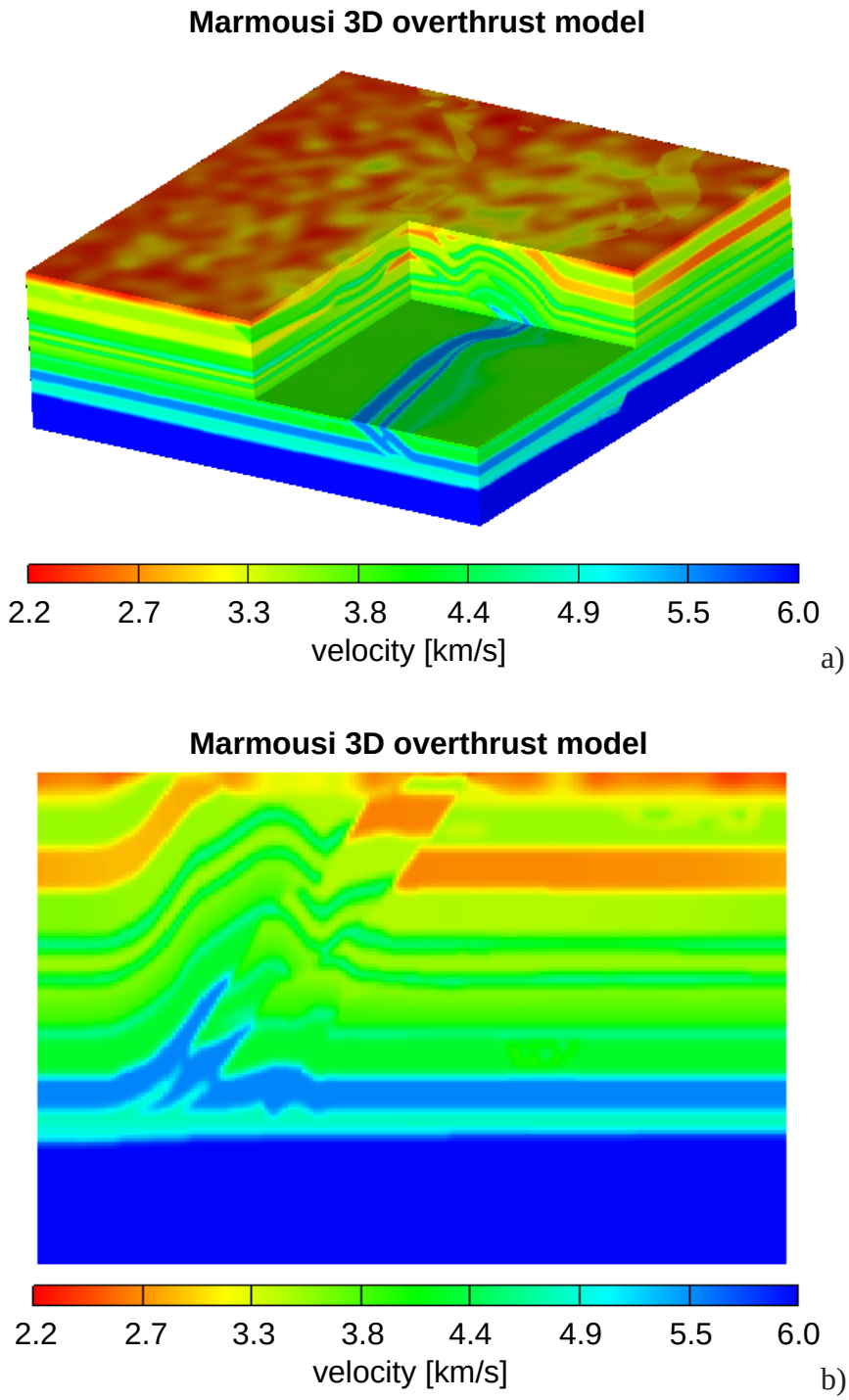

Figure 4.8: Marmousi 3D overthrust model: a) total view and b) slice corresponding to the used 2D data set.

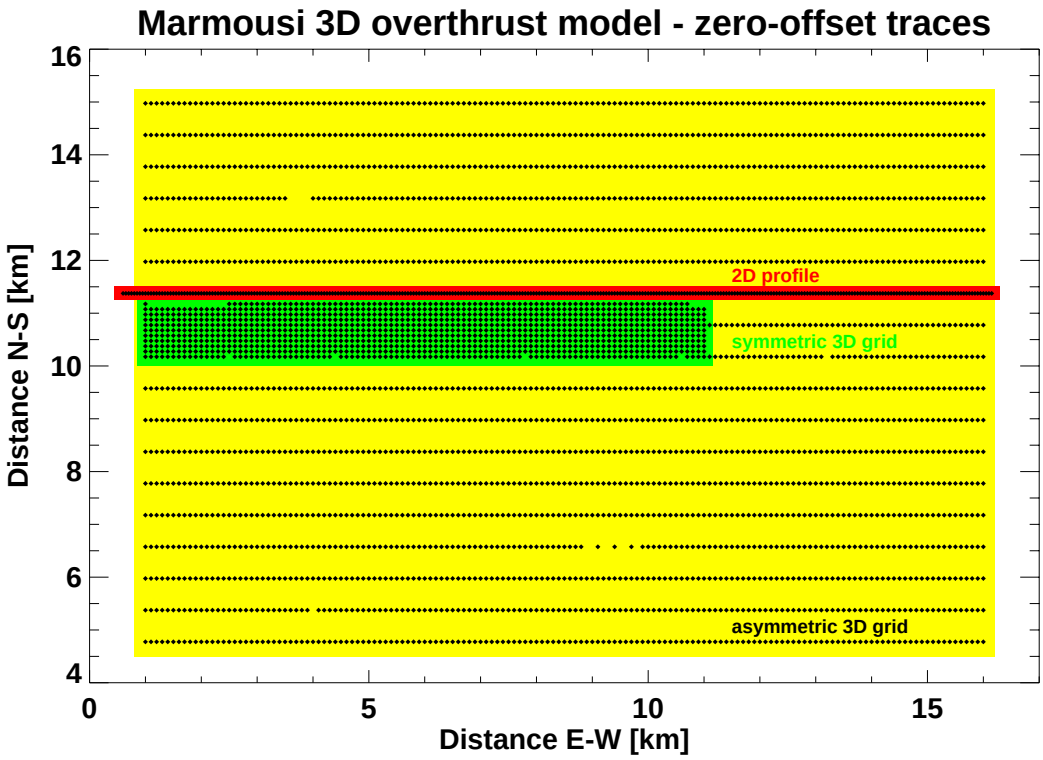

Figure 4.9: Marmousi 3D overthrust model: locations of the zero-offset traces.

domain are much more sensitive to changes in the velocity model than in the time domain there is no point to apply a remigration in the depth domain.

4.2.1 2D data set

We remigrate this comparatively highly resolved data set in the time domain with “normal” velocity and FD operators of max. fourth order in 6000 steps spaced 1 m/s. This covers all velocities found in the model. The zero-offset data set is shown in fig. 4.10, some snapshots of the remigration process are shown in fig. 4.11.

We can distinguish three regions in the data set showing different behaviours during the remigration process:

- In regions with mainly horizontal reflectors nothing changes at all. That is exactly what we would also expect for a conventional migration in the time domain.
- Dipping events at traveltimes greater than approx. 0.5 s vanish with increasing velocity. The overburden is obviously too complex and inhomogeneous to satisfy the assumed homogeneous model. In this case the FD methods does not yield any useful image but indicates that the assumed homogeneity is offended too much.

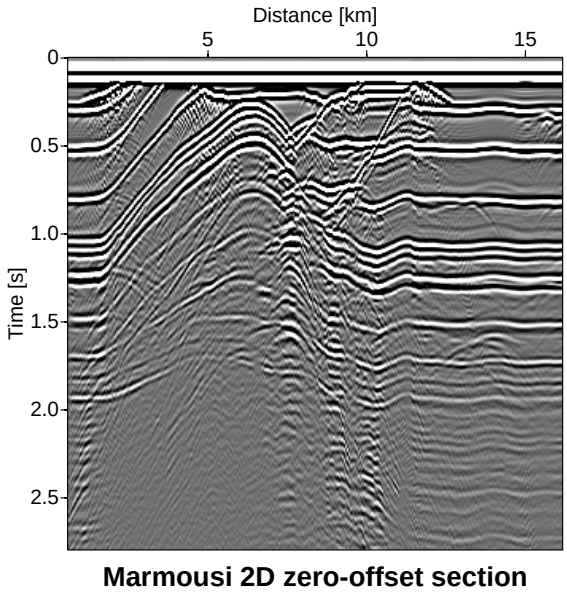

Figure 4.10: Marmousi 2D data set: zero-offset section.

- In the near surface region below approx. 0.5 s we obtain plausible images of the reflectors. By means of the triplications at approx. (0.46 s, 7.6 km) we can estimate the optimum constant migration velocity: we obtain continuous images of the (former) triplications and of the neighbouring structures for $v \approx 2.9 - 3.3$ km/s. The model velocity varies between 3.2 and 3.7 km/s in this region.

Hence, the remigration in the time domain still yields plausible and interpretable results for weakly inhomogeneous media, although it was derived for constant velocities. A too strong inhomogeneity of the model is indicated by the vanishing of dipping reflectors.

4.2.2 Asymmetric 3D data set

This data set is no 3D data set in a strict sense. As we can see in fig. 4.9 we have a distance of 600 m between the lines. Lines are too far apart to get any useful information in cross-line direction.

Therefore, we try to interpolate three additional lines between neighbouring lines to obtain a configuration geometry of 100×150 m^2. The coherency of the events in cross-line direction turns out to be so small at various regions of the data set that we fail to generate continuous images by linear interpolation as well as by bicubic spline interpolation. Another attempt to perform the interpolation in the frequency domain also fails.

After all we apply the remigration in the time domain to the original zero-offset data set without additional interpolated lines. A view of this data set is shown in fig. 4.12a[4]. We can

[4]There seems to be no straightforward way to generate physically significant axes with the software we

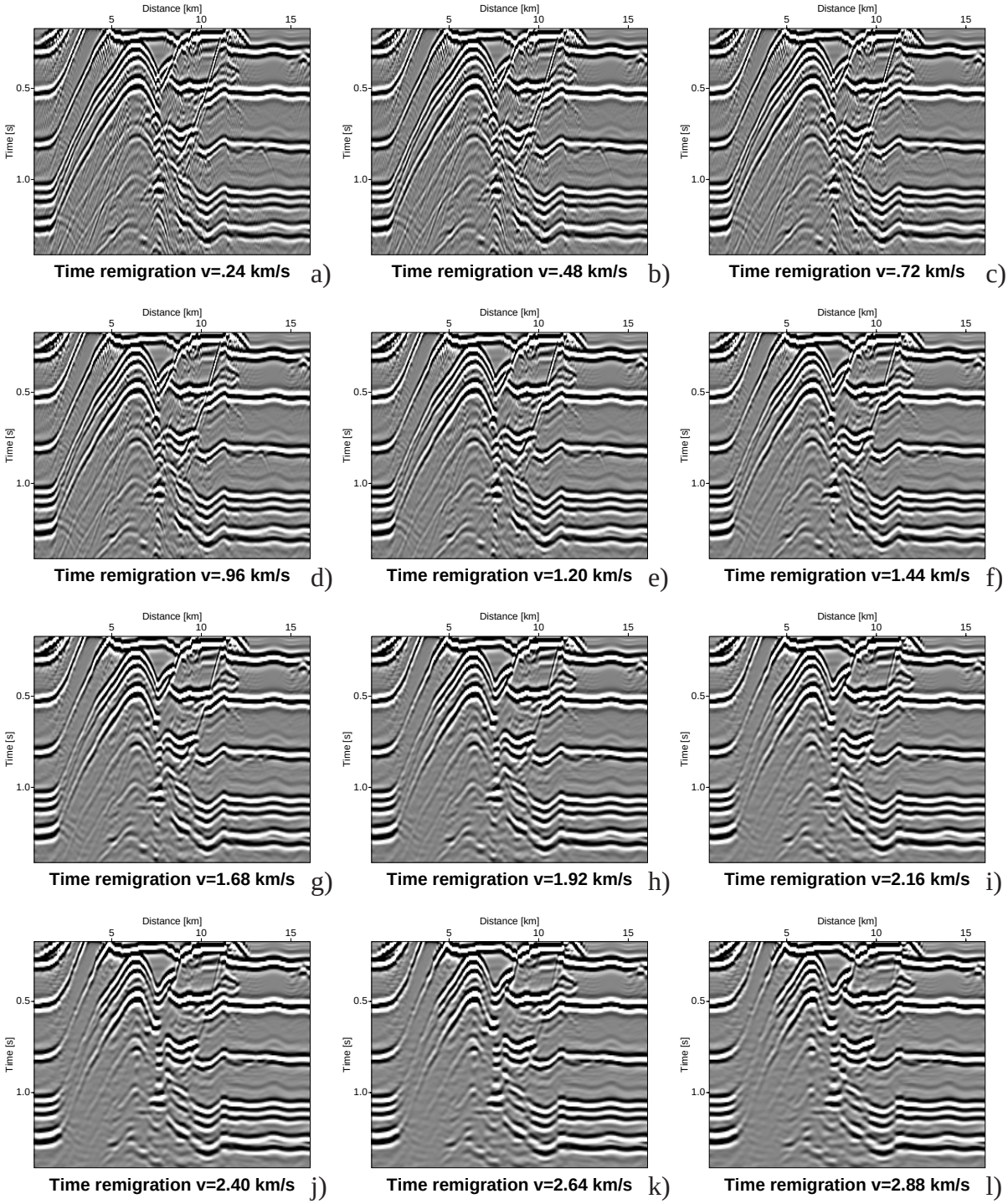

Figure 4.11: Marmousi 2D data set: time-remigrated sections for $v =$ a) 240, b) 480, c) 720, d) 960, e) 1200, f) 1440, g) 1680, h) 1920, i) 2160, j) 2400, k) 2640 and l) 2880 m/s.

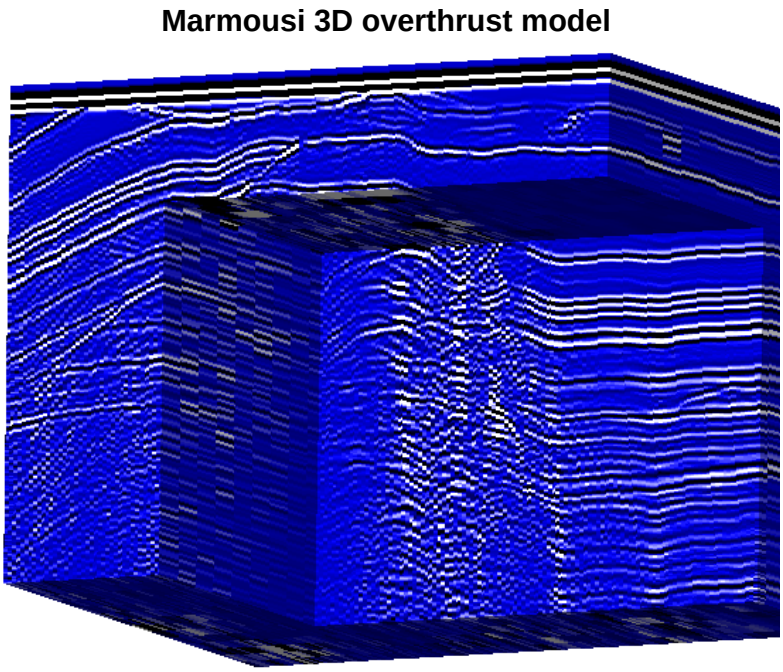

asymmetric 3D zero-offset data set a)

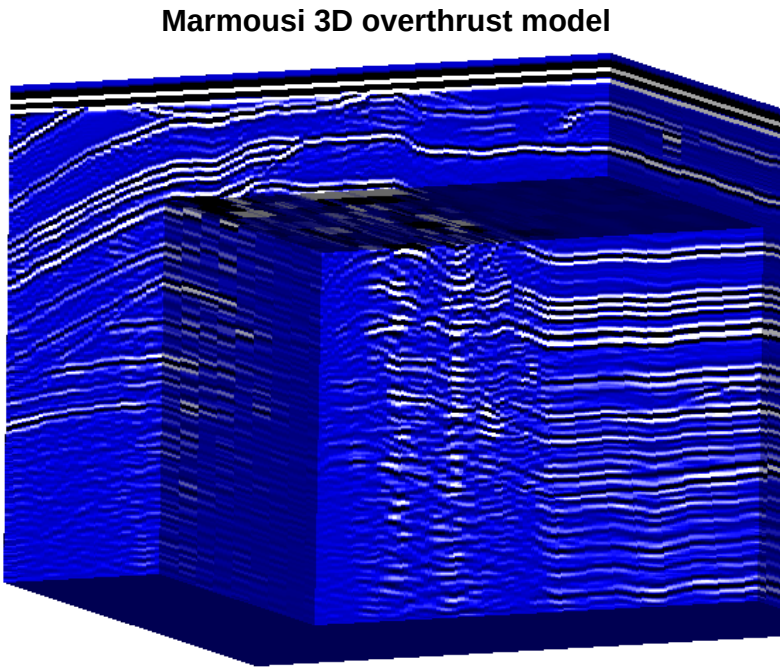

time remigrated section v=2.4 km/s b)

Figure 4.12: Marmousi 3D overthrust model: a) a view of the asymmetric 3D zero-offset data set, b) a view of the snapshot for $v = 2.4$ km/s of the remigration result in the time domain.

hardly see any detailed structures like triplications due to the low resolution of the data set, in particular in cross-line direction.

This zero-offset data set is remigrated in the time domain in 1000 steps spaced 6 m/s with “normal” velocity and FD operators of max. fourth order. The four-dimensional result can hardly be represented on 2D paper. Consequently, only one view of a single snapshot of the remigration process is shown as an example in fig. 4.12b. The complete result has to be interpreted interactively on the screen. Therefore, we have no choice but to describe the result in a few sentences:

If we consider the 3D subsets of the 4D remigration results related to the different lines, we obtain nearly the same results which we would obtain for 2D remigrations applied to each line separately. The very small influence of the neighbouring lines is obviously due to the large distance between the lines.

In this particular case, we can take the 4D result of the 3D remigration as an ensemble of many 3D results of separate 2D remigrations. The application of the 3D FD schemes is just a waste of processing time under these conditions. As was to be expected we observe the same changes of the imaged reflectors as for the previously discussed 2D data set: again we obtain plausible results in the near surface region, whereas dipping events at higher traveltimes vanish with increasing velocity.

4.2.3 Symmetric 3D data set

In contrast to the asymmetric 3D data set we have the same distances between the traces in cross-line and in-line direction. Hence, the symmetric 3D data set is a “real” 3D data set.

Remigration in the time domain is applied in 1000 velocity steps spaced 6 m/s to the zero-offset data set shown in fig. 4.13a with ”normal” velocity and FD operators of max. fourth order. As already mentioned in section 4.2.2 it is hardly possible to print the complete result. We only show one view of a single snapshot of the remigration process in fig. 4.13b.

By interactive interpretation of the result we can observe the same changes we already discussed in section 4.2.2. Unlike for the asymmetric 3D data set the profile lines are no longer independent of each other for this data set: the result of the 3D remigration is no longer equivalent to an ensemble of independent 2D remigration results for each single line. As the Marmousi model mainly varies in the in-line direction the influence of neighbouring lines is anyway small compared to the influence of traces in the same line.

use for the 3D plots, that is why we omit the axes completely.

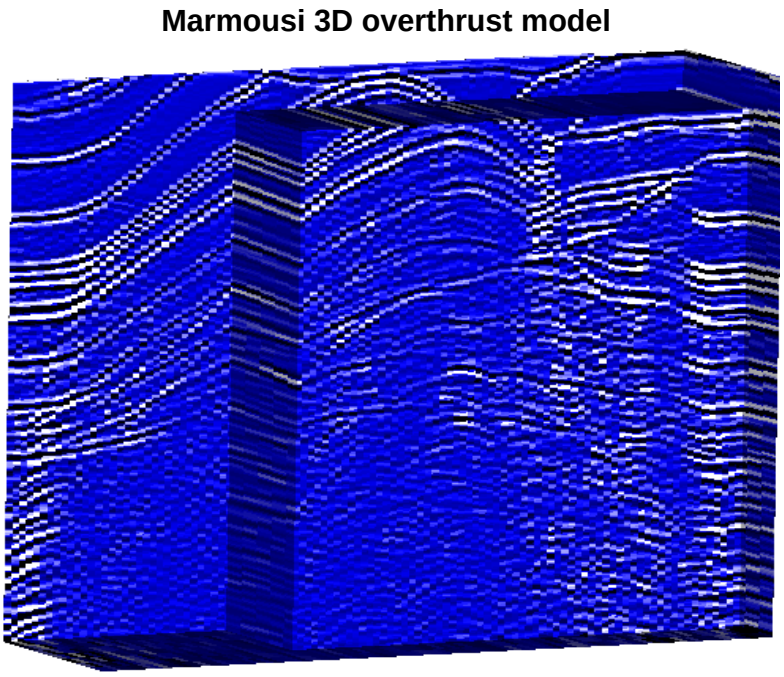

a)

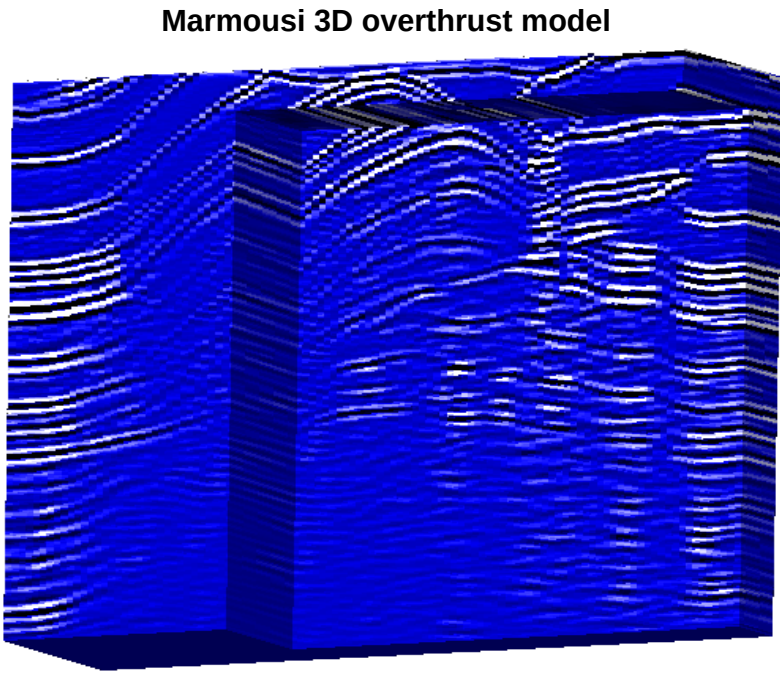

b)

Figure 4.13: Marmousi 3D overthrust model: a) a view of the symmetric 3D zero-offset data set, b) a view of a snapshot of the remigration process in the time domain for $v = 2.4$ km/s.

4.3 Culmitzsch A profile 1560 data set

4.3.1 Acquisition

This hydro-acoustic data set was acquired and provided by DMT GeoTec in Bochum, Germany. The data set was measured on the mine tailings pond Culmitzsch A of the Wismut GmbH near Seelingstädt in Thüringen, Germany. The mine tailings pond is located in a former surface mine which was filled up with mud from the extraction of uranium. More details related to the development of this and of similar old contaminations can be found in Beleites [Bel90] and Paul [Pau91]. A similar data set recorded at the same location was discussed by Schott et al. [SMBN95].

The field equipment shown in fig. 4.14 was moved along the partly crooked line shown in fig. 4.15. The source was a so-called sonic boomer. The response was recorded with a hydrophone in a distance of about 3 m. The source-receiver line was orientated mainly perpendicular to the profile, slightly depending on the influences of wind and water waves. The actual positions were registered by means of GPS receivers and local telemetric systems.

The profile consists of 2506 traces recorded up to 250 ms. The averaged distance between the traces is about 0.67 m. The sampling rate 0.01 ms is extraordinary small, the frequency content is 15 kHz. The raw data set is available in SEPlib format, the geometry is given in a table.

The data set covers numerous very thin and mainly horizontal layers. The impedance contrast at the sea-bottom is very small indicating a weak consolidation of the mud. The floor of the former surface mine is clearly visible in same regions and offers a good opportunity to apply the remigration method.

The raw common-offset data set is not suited to apply the remigration method for several reasons: the remigration programme expects the data on a regular grid, whereas the present data set was acquired along a crooked line at non-equidistant locations. In addition, we would have to apply a normal moveout correction to simulate an approximate zero-offset data set.

4.3.2 Time-migrated data set

Supplementary to the raw common-offset data set, DMT GeoTec also provided a time-migrated data set. According to the available specifications the raw data set was NMO corrected with 1.48 km/s. Subsequently, a spherical geometrical spreading correction with the same velocity was applied, followed by an automatic gain control (AGC) with a time window of 30 ms.

Finally, a time migration with the constant velocity 1.3 km/s was applied to the prepared data set. The result is shown in fig. 4.16 and contains 1682 equidistant traces with a length

Figure 4.14: Field equipment: the sonic boomer is located on the left hand side of the derrick, the hydrophone in the middle. The power source and the computers are located aboard.

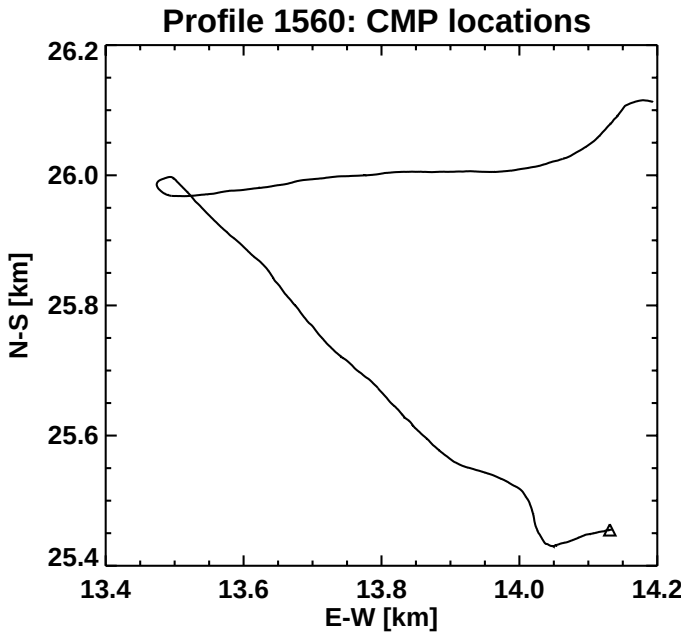

Figure 4.15: Culmitzsch A profile 1560: locations of the common midpoints. The triangle marks the first trace.

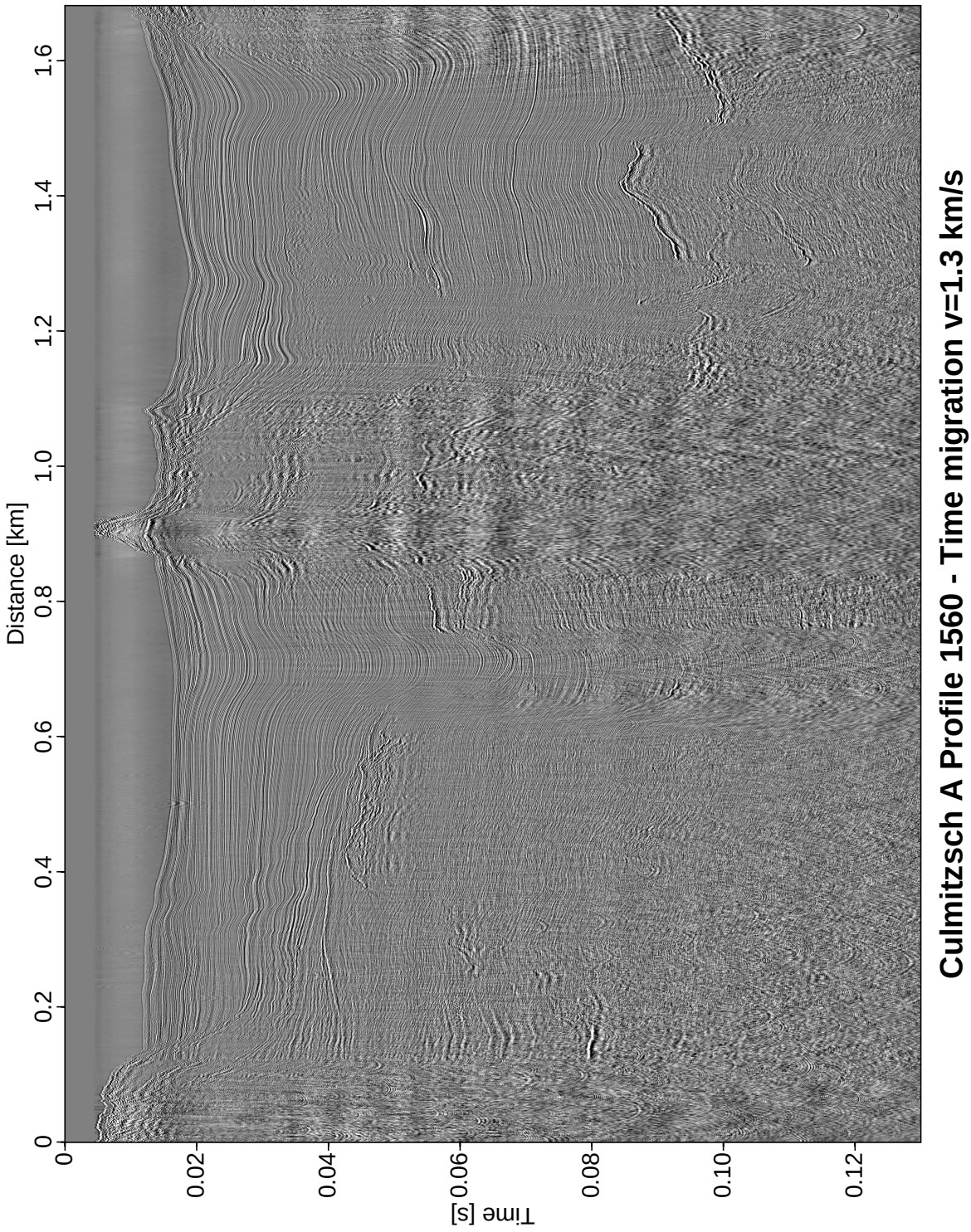

Figure 4.16: Data set Culmitzsch A: time-migrated section for $v = 1.3$ km/s. The profile is partly crooked.

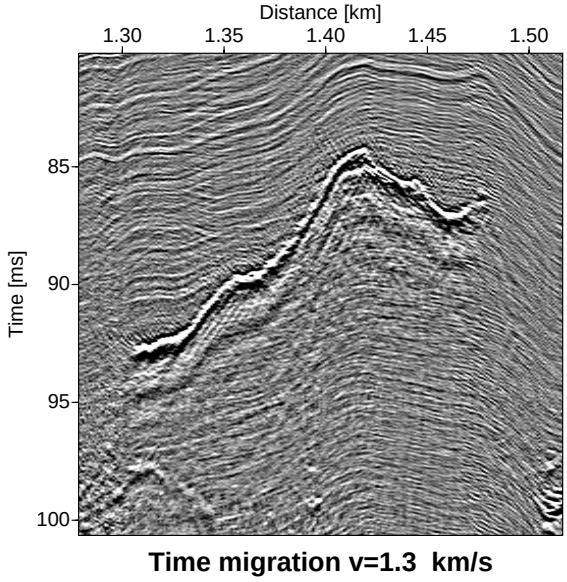

Figure 4.17: Data set Culmitzsch A: subset of the time-migrated section for $v = 1.3$ km/s.

of 130 ms. The sampling rate is again 0.01 ms. This data set is available in SEPlib with separate geometry, too.

Apart from the curvature of the profile all problems which occurred for the remigration of the raw data set are solved if we use the time-migrated data set. However, for small parts of the profile we can take it as an approximately straight line with the exception of strongly curved parts.

Remigration methods are applied to different parts of this data set. The most subsets under consideration turn out to be more or less insensitive to velocity changes. In regions with larger dips we obtain of course changes but it is impossible to estimate an optimum constant migration velocity because significant structures like triplications and diffraction patterns are missing. This means that all remigrated sections are likewise plausible for realistic velocities.

In fig. 4.17 a subset of the time-migrated sections is shown for which the remigration yields interpretable results. The strong event in this subset is a reflection from the floor of the former surface mine.

We apply the remigration in the domain to this subset in two separate processes with the initial velocity $v_0 = 1.3$ km/s, on the one hand with 1000 steps and $\Delta v = 1$ m/s, on the other hand with 1300 steps and $\Delta v = -1$ m/s. We use “normal” velocity and FD operators of max. fourth order.

Both remigration results and the initial data set are merged to one data set covering velocities between 0 (equivalent to the zero-offset section) and 2.3 km/s. Some sections of this merged data set are shown in fig. 4.18. It is no longer recognizable that this data set was computed in two separate processes, we are unable to identify the initial data set in the

result. According to this we can take the sections in fig. 4.18 as snapshots of *one single* remigration process.

The image of the floor of the former surface mine significantly changes during the remigration process. Most noticeable are the hyperbolic smiles above the reflector for velocities higher than approx. 2 km/s. They indicate a too high migration velocity. For lower velocities we observe structures below the left hand side of the reflector which we interpret as so-called frownings. For the optimum constant migration velocity neither smiles nor frownings should be visible. We observe the smallest artifacts of these kinds in the figs. 4.18g and 4.18h. In this way we can estimate the optimum constant migration velocity to range between 1.7 and 1.8 km/s.

The unavoidable noise in real data sets has obviously no consequences for the applicability of the remigration programme. This was already shown for noisy synthetic data sets by Jaya et al. [JSH96].

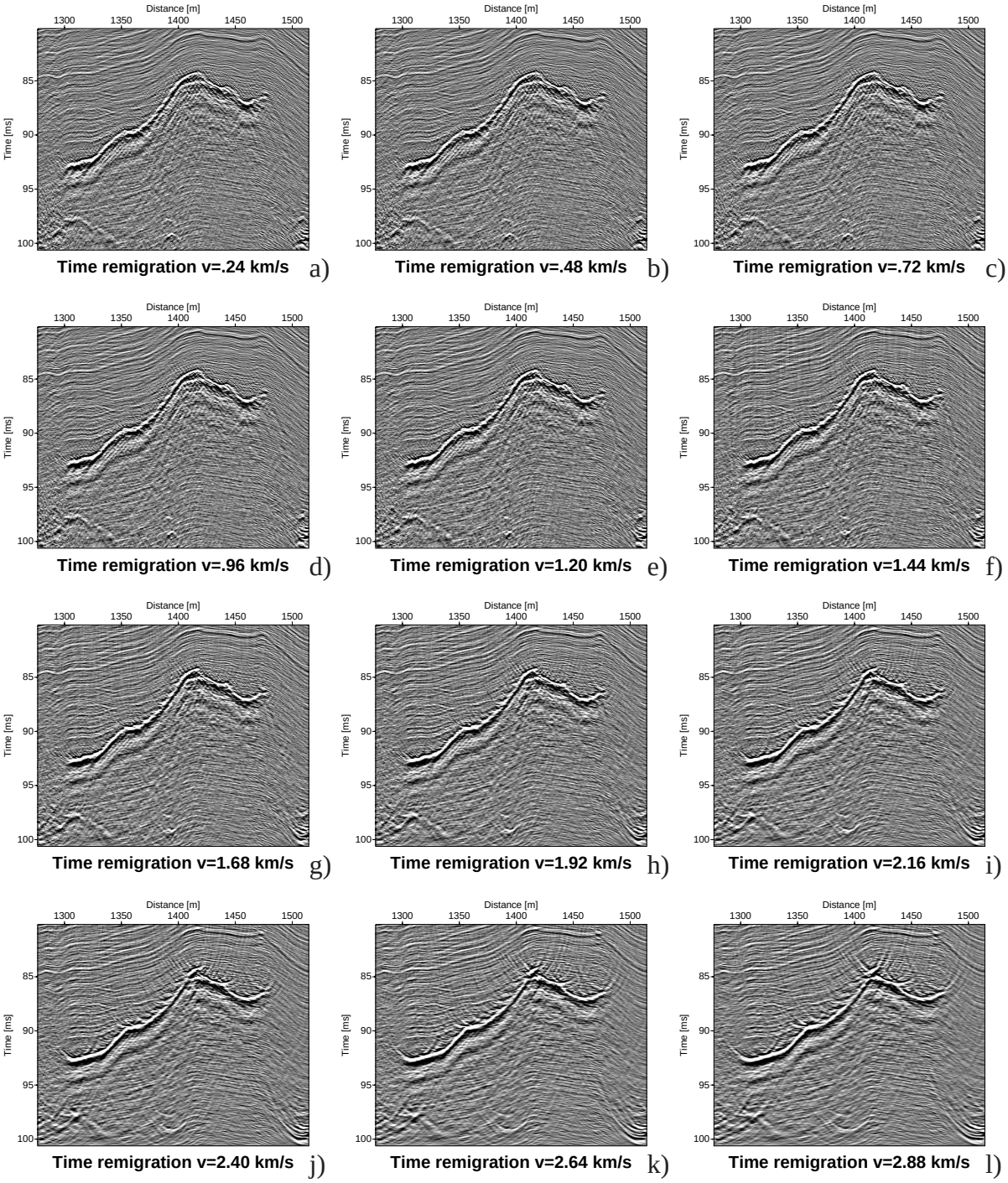

Figure 4.18: Data set Culmitzsch A: time-remigrated section for v = a) 240, b) 480, c) 720, d) 960, e) 1200, f) 1440, g) 1680, h) 1920, i) 2160, j) 2400, k) 2640 and l) 2880 m/s.

Chapter 5

Application of the NMO/DMO/MZO program

5.1 Application of the NMO/DMO

5.1.1 Noise-free synthetic data set

To test the implementation, we use a simple model with a dome-like structure as shown in fig. 5.1a. Several common-offset sections are simulated for this model by means of a program of the Seismic Unix package based on the exploding reflector method. One of this common-offset sections is shown in fig. 5.1b. Each common-offset section consists of 201 traces spaced 10 m with 321 samples and a sampling rate of 2.5 ms. We generate sections for seven different offsets between 100 and 400 m. The constant velocity above the reflector is 2.5 km/s. We use a Ricker wavelet with a main frequency of 60 Hz.

We apply a NMO correction with $v = 2.5$ km/s to this data set including a geometrical spreading correction[1]. Areas with a pulse stretch greater than 25% of the wavelet length are muted.

The slice through the common-offset gather parallel to the offset axis in fig. 5.2a illustrates the influence of the offset on the traveltimes. In fig. 5.2b the same slice is shown after the NMO correction. For the chosen midpoint $\xi = 0$, i. e. for the horizontal apex of the dome, the NMO correction immediately yields the correct result. The pulse stretch caused by the NMO correction is clearly visible.

For dipping segments of the reflector it stands to reason that the NMO result still depends on the offset. The offset depend traveltimes are shown in fig. 5.3a for a midpoint at the flank of the dome. The difference of the NMO corrected traveltimes and the correct zero-offset

[1]The geometrical spreading correction is applied for line sources in 2D. A correction for point sources in 3D is also available.

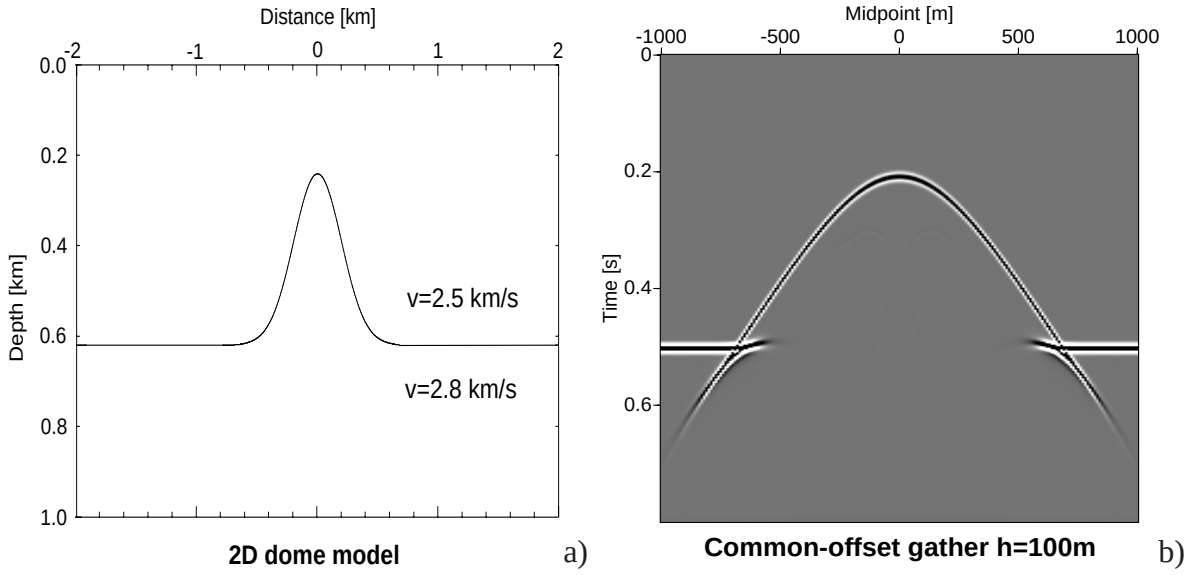

Figure 5.1: a) Model with a dome-like interface, b) common-offset section for $h = 100$ m.

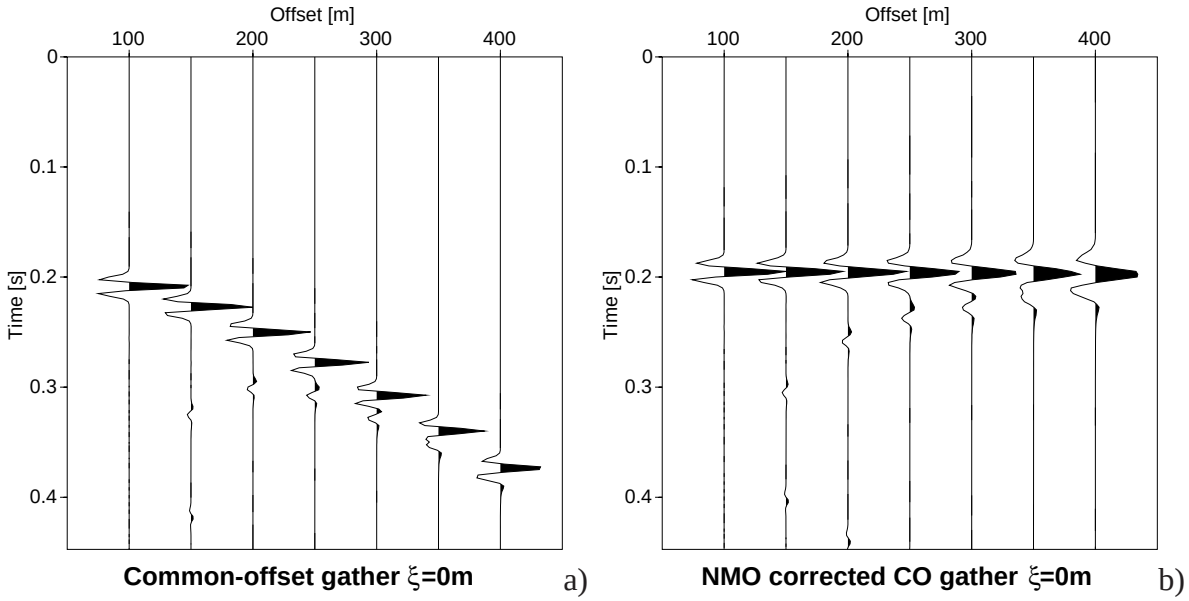

Figure 5.2: Slice through the common-offset data set a) before and b) after the NMO correction for a horizontal reflector segment.

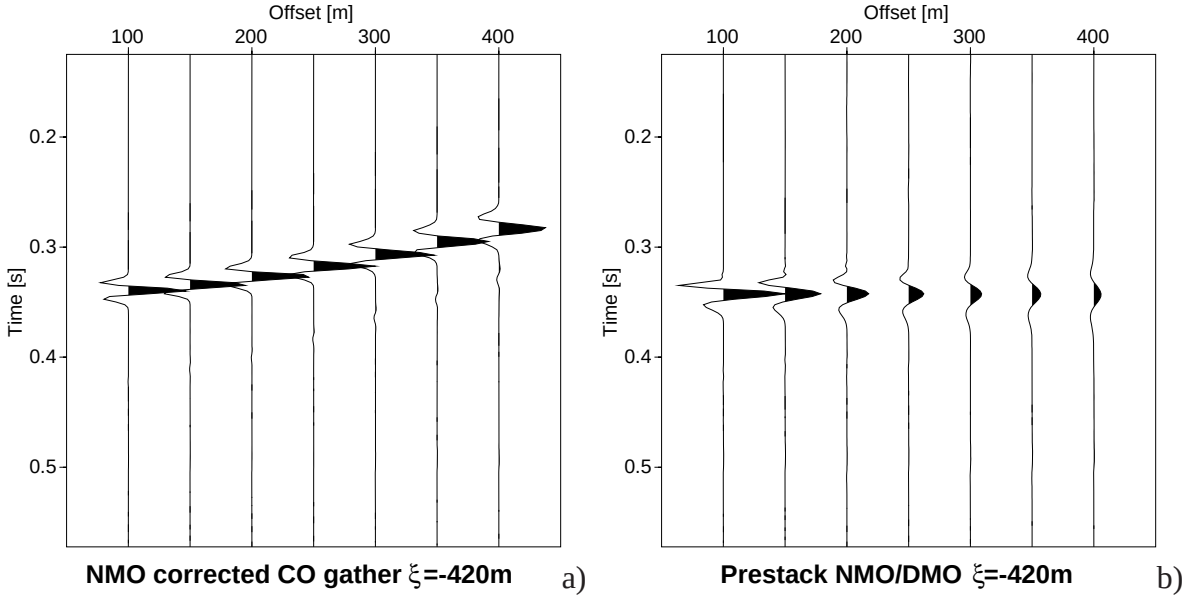

Figure 5.3: Slice through the common-offset data set a) after the NMO correction and b) after the DMO process at the flank of the dome.

traveltimes increases with increasing offset and—not shown in this figure—with increasing dip.

The unstacked simulated zero-offset sections computed with a NMO/DMO process are shown in fig. 5.3b for one midpoint ξ at the flank of the dome. The influence of the dip on the traveltimes is entirely corrected, though the amplitudes decrease with increasing offset and increasing dip due to grid dispersion. The DMO process is applied with a maximum[2] of 500 offset steps spaced 0.8 m.

Some snapshots of this DMO process are shown in fig. 5.4. We apply the DMO separately for each initial offset h_0 and stack all results with identical values of the propagation variable h. With decreasing offset h more and more common-offset sections contribute to the stack, the entire initial data set contributes to the stack for $h \leq h_{0\min}$. The DMO correction generates only very small artifacts, the visible artifacts originate from the input data set. All common-offset sections interfere constructively in the stack indicating the consistency of the method.

5.1.2 Noisy synthetic data set

We define another model with a dome-like interface and generate a synthetic common-offset data set with 16 offsets spaced 12.5 m. The smallest offset is $h = 0$. Each section consists of 121 traces spaced 25 m with 301 samples and a sampling rate of 4 ms. Contrary

[2]The maximum number of offset steps applies to the largest offset in the initial data set. For the subsequent stacking we require constant offset steps Δh implying a smaller number of offset steps for smaller offsets.

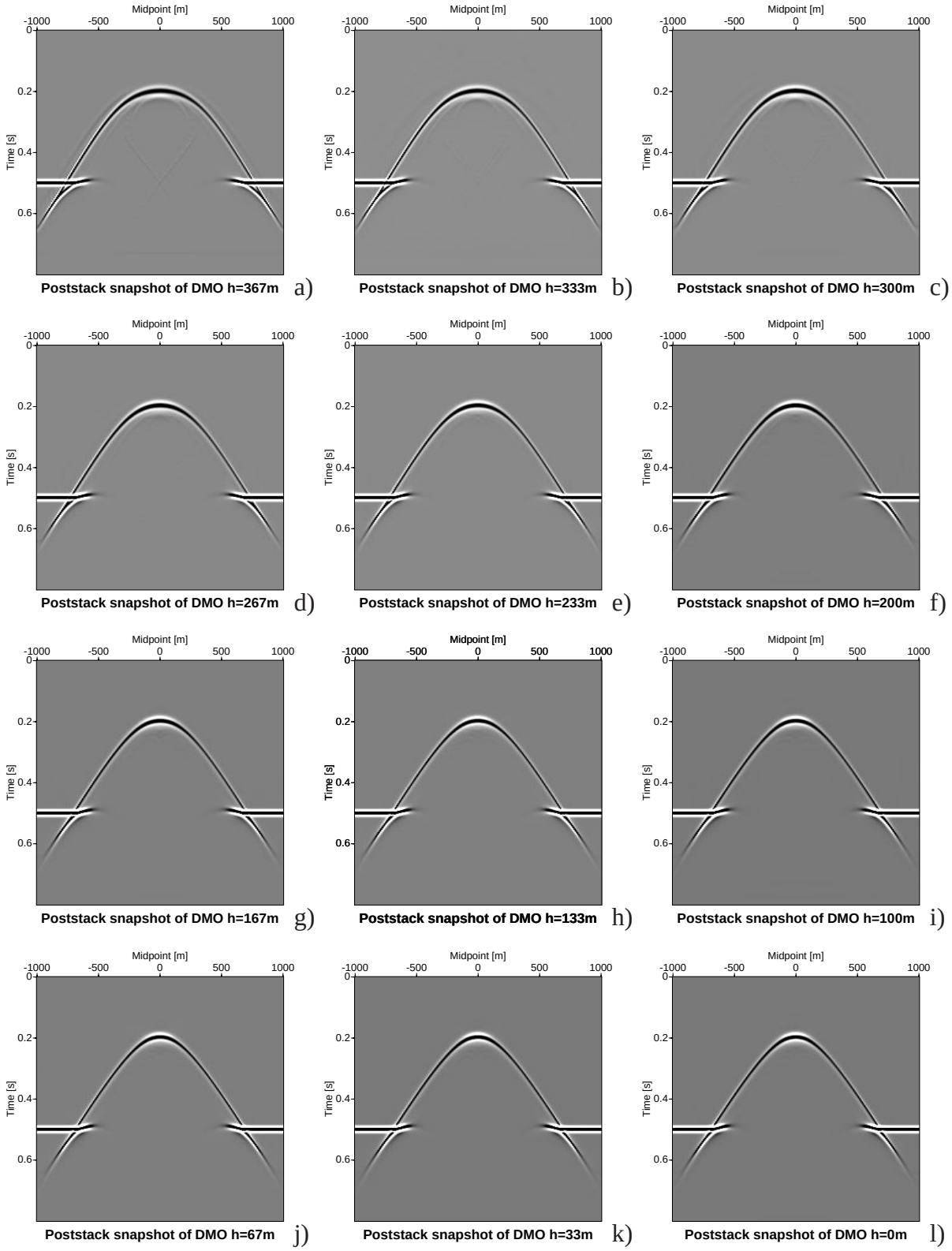

Figure 5.4: Post-stack snapshots of the DMO process for $h =$ a) 367, b) 333, c) 300, d) 267, e) 233, f) 200, g) 167, h) 133, i) 100, j) 67, k) 33 and l) 0 m.

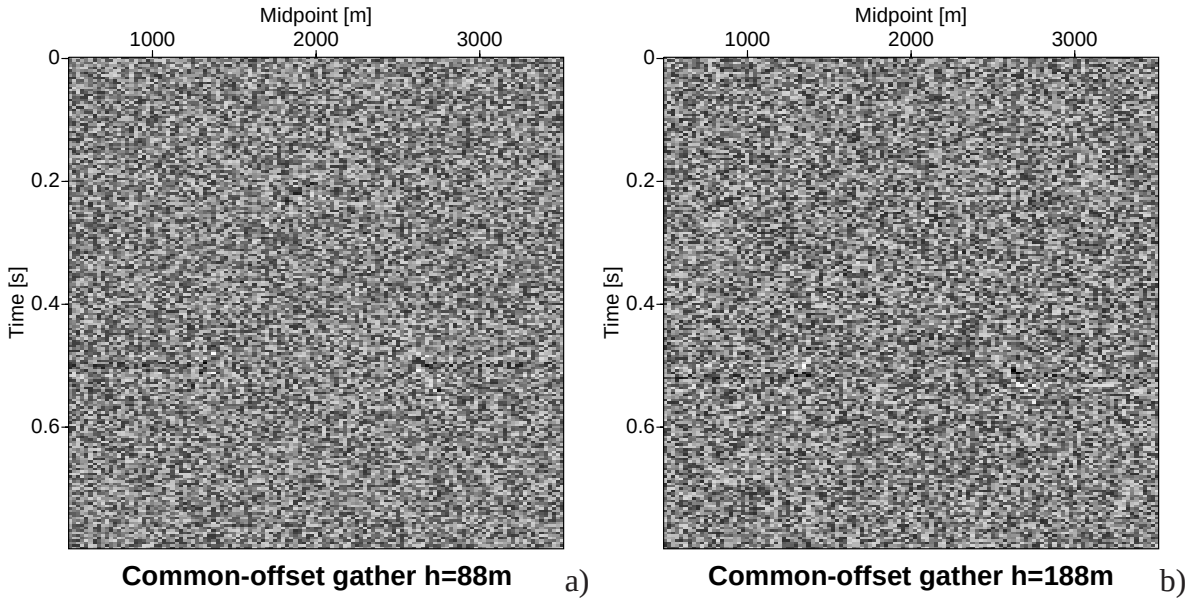

Figure 5.5: Common-offset section of the noisy data set for a) $h = 88$ and b) 188 m.

to the data set in section 5.1.1 we use a ray tracing program of the $AMIG$ package [Han95] to compute the traveltimes. By means of the program synseis of the same package we simulate the seismograms using a Gabor wavelet with a main frequency of 60 Hz. Finally, we add synthetic noise with a signal/noise ratio of 1:1.

Two sections of the data set are shown in fig. 5.5. We can hardly see the dome in this figure as well as in all other sections. Only the horizontal parts are slightly visible.

The data set is NMO corrected with the true model velocity including a geometrical spreading correction and the muting of areas with a pulse stretch greater than 25% of the wavelet length. The DMO process with a maximum of 500 offset steps spaced 0.375 m and subsequent stacking yields a clear image of the reflector. As more and more information is available with decreasing offset, the signal/noise ratio increases with decreasing offset. The visible edge in the data set is due to the muting operation and causes some artifacts which are not relevant in this particular case. The may be reduced or even eliminated by applying a smooth taper at the edge of the muted area during the NMO correction.

5.2 Application of the MZO

5.2.1 Noise-free synthetic data set

The MZO in its original form proved unstable with all parameter and data sets under consideration so far. To get on the track of this problem, we generate a small synthetic data set and simplify the FD scheme as far as possible:

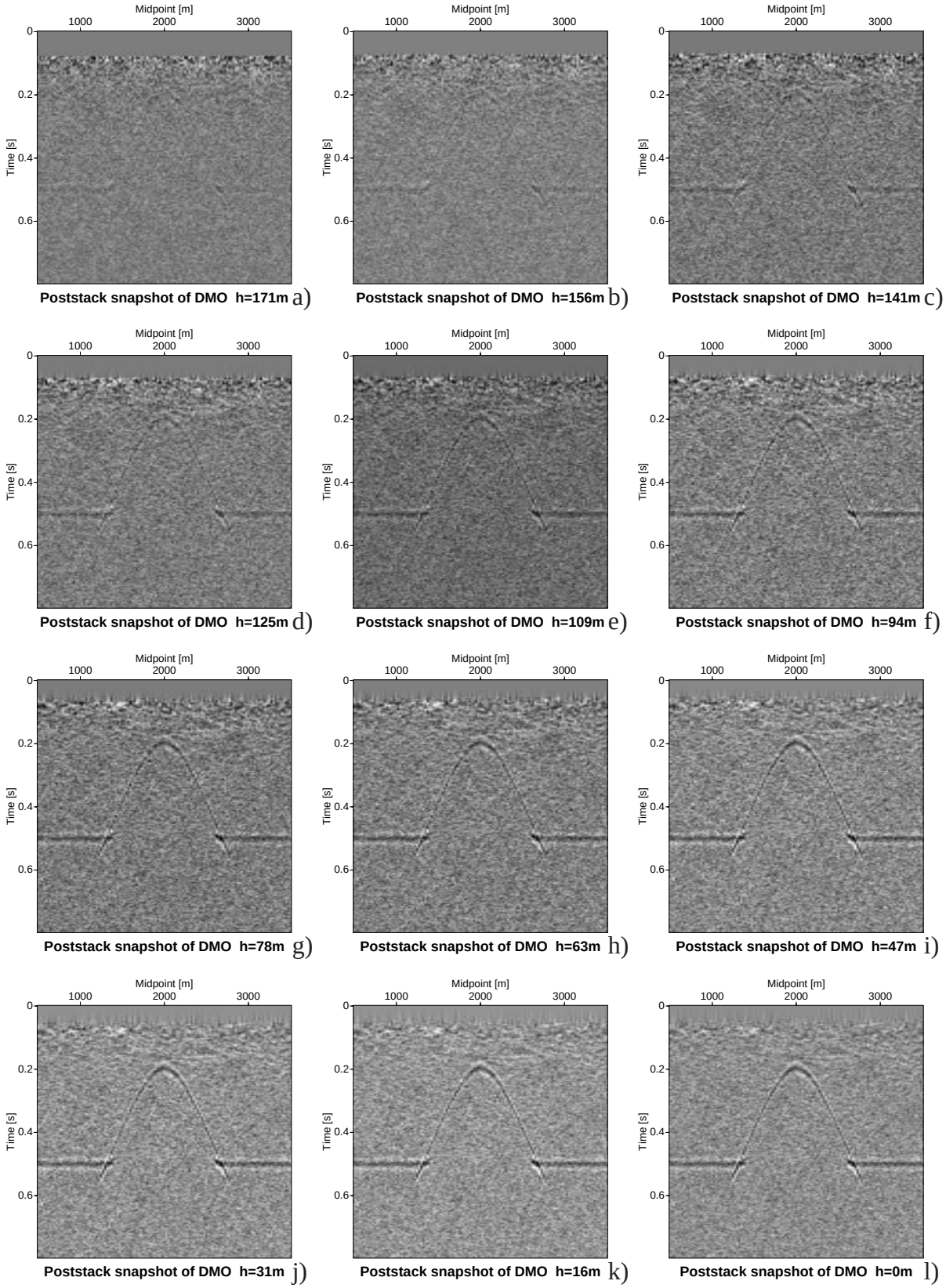

Figure 5.6: Post-stack snapshots of the DMO process for $h =$ a) 171, b) 156, c) 141, d) 125, e) 109, f) 94, g) 78, h) 63, i) 47, j) 31, k) 16 and l) 0 m.

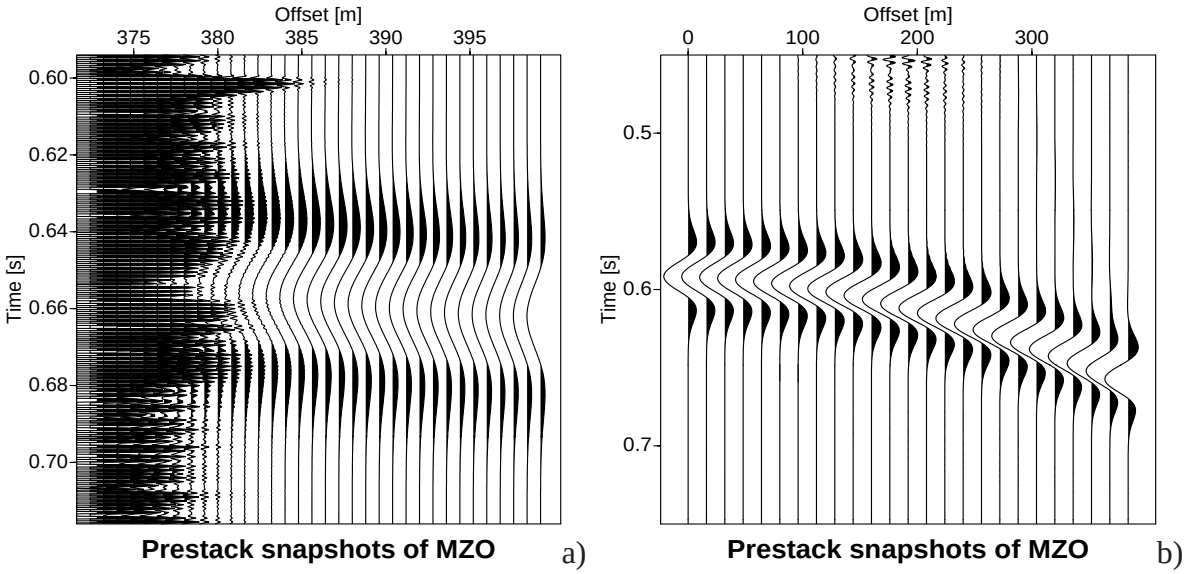

Figure 5.7: Detail of pre-stack MZO snapshots a) without and b) with smoothing.

The model consists of a single plain reflector. We convolute the model with a Ricker wavelet with a main frequency of 30 Hz to simulate a synthetic seismogram. For this horizontal model without any dip the MZO problem reduces to the NMO correction. The data set contains only one offset $h = 400$.

We simplified the FD scheme by omitting the partial derivative $\partial^2/\partial\xi^2$. This reduces the problem to a one-dimensional problem and eliminates the influences of the edges of the computational space. Under these conditions we expect to obtain exactly the same travel-times as NMO correction would yield, too.

In spite of these simplifications the MZO is still unstable. The detail of the MZO result in fig. 5.7a illustrates the problem: strongly increasing high frequency artifacts occur with decreasing offset. This effect seems not to depend on the discretization intervals and is reminiscent of similar results for the remigration in depth domain in section 4.1.2.

Picking the zero-crossings of the wavelet in the MZO result, we observe that the wavelet length decreases from 25 ms for $h = 400$ m to 23.5 ms for $h = 383$ m. The frequency of the wavelet increases with decreasing offset. As already discussed for the remigration in the depth domain this leads to instability.

For the remigration in the depth domain with $\Delta v < 0$ we expect an increasing frequency content, whereas we cannot explain this phenomenon for the MZO which is reduced to a pure NMO correction in this case.

By smoothing the traces after each offset step we can reduce the high frequency artifacts. A very simple smoothing operator, i. e. a linear combination of three neighbouring samples, leads to stable processes under certain conditions. This smoothing operator is discussed in appendix B. The data set shown in fig. 5.7b is generated with a smoothing parameter

$s = 0.32$. This is equivalent to a convolution with the discrete operator $(0.32;1;0.32)/1.64$. The larger the smoothing parameter, the more stable the process and the larger the stretch of the wavelet. We chose the smallest value of s just yielding a stable process.

Of course, the smoothing also affects the approximations of the first and second order derivatives with respect to the time in the FD scheme (3.8). Therefore, we have to expect a result depending on the smoothing operator.

At first glance, the result computed in this way looks promising: the frequency of the wavelet hardly changes, the relation between the traveltime and the offset seems to be hyperbolic as we would expect for a pure NMO correction. However, a closer look exposes totally wrong traveltimes: for the initial value $t(h = 400\text{m}) = 649.5$ ms and the model velocity $v = 2500$ m/s we have an analytic zero-offset traveltime $\tau = t(h = 0\text{m}) = 565.2$, but the MZO yields $\tau = 578$ ms. As necessary for the stability, the wavelet gets slightly stretched during the MZO process. The mentioned values are related to the upper zero-crossing of the wavelet which can easily be picked.

It is near at hand to hold the smoothing operator responsible for this discrepancy, and indeed the discrepancy increases with increasing smoothing parameter. But obviously the values not only deviate due to the smoothing: comparing the MZO results with and without smoothing is only possible for a small range of offsets but yields significant traveltimes anyway. For an offset of $h = 383$ m we find 645 ms with smoothing, 644.5 ms without smoothing, and 643 ms analytically. Even without the smoothing operator the traveltimes deviate from the analytical values after a few offset steps.

For the sake of completeness we apply the MZO with smoothing to the noise-free common-offset data set used in section 5.1.1. The stacked result is shown in fig. 5.8. As we have to expect we obtain no constructive interference of the simulated sections. With each new common-offset section contributing to the stack the images splits furthermore. The empirically determined smoothing parameter for this data set is $s = 0.029$.

The stabilizing smoothing operator is applied trace by trace. Consequently, we assume that one of the derivatives with respect to the time in the MZO image wave equation (2.54), in particular the second order derivative, causes the instability. To obtain a better approximation of this second derivative, we try to calculate this derivative in the frequency domain:

We apply a fast Fourier transformation (FFT) with respect to the time after each offset step. In the frequency domain we can only compute the second derivative $\partial^2/\partial t^2$, the calculation of the mixed derivative $\partial^2/(\partial t\,\partial h)$ is impossible due to the semi-explicit FD schemes, because we would have to calculate $\frac{\partial}{\partial h}(\partial p^{l+1}/\partial t)$.

To calculate the second derivative, we proceed as follows: after each offset step we pad each trace $p^l_{i,j}\ \ \forall\, i\ (l, j = const)$ with zeros in that manner that we obtain a number of samples $n_{\text{fft}} = 2^{[2+r(\log_2 n)]} = 2^{[2+r(\ln n/\ln 2)]}$. In this equation the function r denotes the nearest natural number greater than the argument of r.

Subsequently, we transform the data set to the frequency domain trace by trace by means

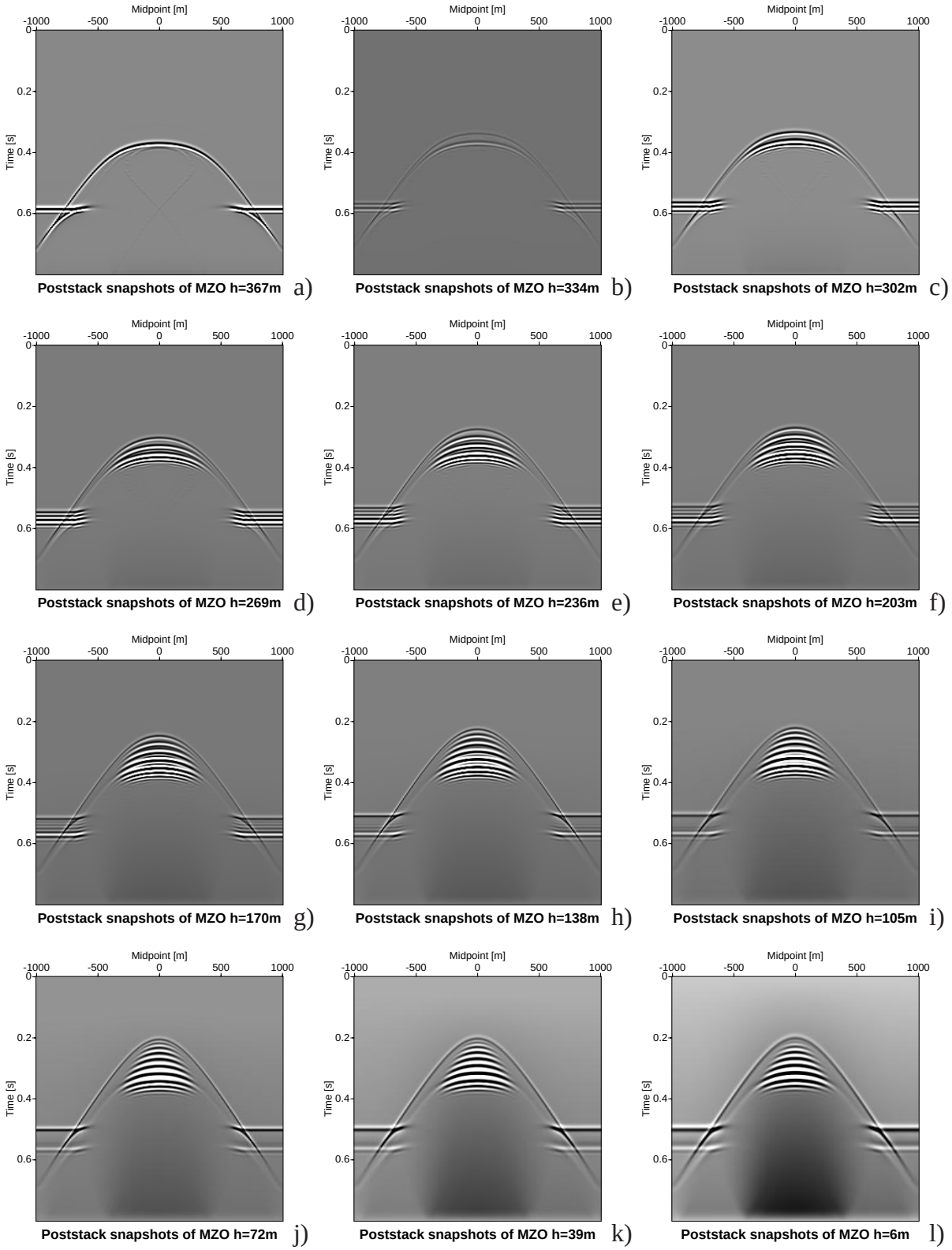

Figure 5.8: Post-stack snapshots of the MZO process with smoothing for $h =$ a) 367, b) 334, c) 302, d) 269, e) 236, f) 203, g) 170, h) 138, i) 105, j) 72, k) 39 and l) 6 m. There is no constructive interference of the simulated sections.

of a FFT program by Press et al. [PTVF86], multiply it by an operator Ω, and return to the time domain.

This yields an array of second derivatives with respect to the time for all traces and times we use to replace the second expression in equation (3.8). The padded zeros reduce the aliasing effects due to the discrete Fourier transformation by shifting them to higher traveltimes outside the region of interest.

The used operator has the analytical form $\Omega = -\omega^2$, discrete and under consideration of the current representation of the frequency values for the FFT we obtain a real-valued vector

$$\Omega = \left(0, -\frac{2\pi}{n_{\text{fft}}^2}, -\frac{4\pi}{n_{\text{fft}}^2}, \cdots, \frac{-2\pi\,(n_{\text{fft}}-1)}{n_{\text{fft}}^2}, \frac{-2\pi n_{\text{fft}}}{n_{\text{fft}}^2}, \frac{-2\pi\,(n_{\text{fft}}-1)}{n_{\text{fft}}^2}, \cdots, -\frac{2\pi}{n_{\text{fft}}^2}\right) . \qquad (5.1)$$

The expression $-2\pi n_{\text{fft}}/n_{\text{fft}}^2$ is the vector element no. $n_{\text{fft}}/2+1$.

The numerous transformations required for the application of this operator lead to considerably higher computational cost than the much simpler FD operators. Although this method is more precise than the FD operators, the behaviour of the MZO process hardly changes: instability and wrong traveltimes still occur. Therefore, the attempt to solve the initial value problem for the MZO also fails and is not discussed any further.

Unfortunately, we have to conclude that the recent implementation of the MZO is not applicable, as it always leads to either instability or wrong traveltimes.

Chapter 6

Conclusion

6.1 Remigration

For homogeneous models the remigration both in the time and in the depth domain yields kinematically correct results for the true model velocity. Apart from grid dispersion effects occurring in particular in the vicinity of steep flanks, the results are comparable to the results of conventional migration methods.

The grid dispersion is a purely numerical effect and may be reduced by using a finer grid for the discretization and/or more accurate FD operators of higher order. The discussed implementation is far from being exhausted in this respect. The interpolation of additional traces and samples may also be used to improve the results.

A decisive advantage of the remigration compared with conventional migration methods is the fact that an arbitrary number of images for many different velocity models can be computed in one single process.

For the implemented FD schemes only the numerical resolution of the computer sets a lower limit for the possible velocity steps: for too small Δv the finite differences will vanish or get to inaccurate. This never happened for the cases under consideration so far. As a matter of fact several hundred or thousand velocity steps are sufficient to obtain good results. A further decreasing of the step size does not lead to better results, the intrinsic resolution of the computer is far higher than the required values.

The computational costs for an entire sequence of images is of the same order as for conventional migration methods calculating only *one single* migrated image. Hence, the remigration is a fast and efficient method for the generation of many migrated images.

A sequence of migrated images for a entire range of model velocities enables us to apply interpretation methods which are quite costly with conventional methods: it is possible to observe the (nearly continuous) propagation of the seismic images through the fictitious

$(v,\vec{x})$- or (v,x,y,t)-domain, respectively. In this way we can estimate the sensitivity of the images to changes of the model. Furthermore, the optimum constant migration velocity may be estimated by means of certain criteria like the continuity of the images, vanishing triplications, or collapsing diffraction patterns. However, this implies that such structures have to occur in the data set and/or the continuity of the images significantly changes, otherwise the velocity estimation is hardly possible.

In the framework of this thesis all derivations are restricted to homogeneous models. This is a crucial restriction for the application. As discussed for the Marmousi 3D overthrust model, the method is also applicable to weakly inhomogeneous models with certain restrictions. Dipping events vanishing with increasing velocity indicate whether the model is too inhomogeneous or not. As the remigration in the depth domain is much more sensitive to velocity changes its application to inhomogeneous models is not recommended.

In principle the derivation of the seismic image wave equations may be generalized for other simple models, e. g. models with a vertical velocity gradient, but we can hardly expect to obtain straightforward image wave equations by all means. This problem remains for future research.

The remigration in the time domain turned out to be a stable and useful tool for the processing of post-stack data sets. As the remigration velocity $v = 0$ is related to the (simulated) zero-offset section, remigration in the time domain can be applied to migrated as well as unmigrated data sets. Time remigration is possible towards higher or lower velocities without problems.

The remigration in the depth domain is applicable with certain restrictions. The frequency content of the data set varies with the velocity as expected: it decreases with increasing velocity and vice versa. This leads to the instability of the implemented FD schemes towards lower velocities. Another problem is the mainly vertical propagation of the imaged reflectors in the depth domain. The computational space must be chosen large enough to enclose all images for all velocities under consideration, otherwise some of the imaged reflectors will leave the computational space and cause artifacts due to the semi-explicit properties of the FD schemes.

For purely kinematical studies and homogeneous models it is straightforward to transform a data set from the time to the depth domain and vice versa. Hence, every actual remigration problem may be solved in the time domain and subsequently be transformed to the depth domain to avoid the problems in the depth domain. As the transformation depends on the velocity, we cannot transform the entire result but have to transform each single section of it separately with the corresponding velocity.

6.2 NMO, DMO and MZO

A chained NMO and DMO with subsequent stacking yields the expected results for the homogeneous models under consideration: the zero-offset sections separately simulated for each initial offset are kinematically very close to the actual zero-offset section. As the NMO and the stacking procedure are performed in a conventional way we will not discuss them any further.

The actual DMO propagation process is numerically very stable and generates very few artifacts, merely the amplitudes decrease with decreasing offset due to grid dispersion. Therefore, the higher the initial offset, the smaller the contribution of the related common-offset section to the stacked section. This may be controlled by a weighted stack.

As for the remigration, the usage of smaller discretization intervals and more accurate FD operators of higher order should reduce the grid dispersion. In the DMO process only the amplitudes are changed due to dispersion in contrast to the remigration with its kinematically relevant artifacts.

The DMO yields numerous images for an entire range of offsets $h_{\max} > h \geq 0$ with small computational costs. Once again it is possible to observe the quasi-continuous propagation of the seismic images in the fictitious (ξ, τ)-domain. In this way the sensitivity of the image to offset variations can be estimated.

The MZO without additional smoothing turned out to be unstable under all considered conditions. This behaviour seems not to depend on the chosen discretization intervals and other parameters. After a strong simplification of the problem for a 1D model for which the MZO reduces to a NMO problem we observed two phenomena: on the one hand we obtain too high traveltimes compared with the analytical results, i. e. the images propagate to "slow", on the other hand the frequency content of the data set increases with decreasing offset.

The implemented FD schemes are unstable for increasing frequency content as we already observed for the remigration problem in the depth domain. For the remigration in depth domain we expect this behaviour, whereas we cannot explain this effect for the MZO problem.

The MZO process can be forced to be stable by suppressing the highest frequencies by means of a smoothing operator depending on a parameter to be determined empirically. However, this causes the seismic images to propagate even slower, the anyway too high traveltimes deviate even more from the analytical values. Therefore, the MZO is not applicable even if we force the process to be stable.

Similar to the remigration problem for which we can avoid the problems in the depth domain by a transformation of the data set to the time domain, we can use the DMO correction instead of the MZO. The transformation between the (ξ, t)- and the (ξ, τ)-domain is given by the NMO correction. By analogy with the remigration we can transform DMO-corrected

sections back into the (ξ, t)-domain separately for each offset by means of an inverse NMO.

This enables us to simulate not only zero-offset and NMO-corrected common-offset sections but also (uncorrected) common-offset sections.

6.3 Prospects

The discussed methods offer a lot of opportunities for future research. Some of them are listed below very briefly:

- Extension of the theory for simple inhomogeneous models
- Solving the initial value problems with other methods as e. g. in the frequency domain
- Application of more accurate FD operators of higher order
- Better handling of the edges of the computational space, e. g. by means of absorbing regions at the edges
- A more efficient implementation. The FD schemes are well-suited for parallel processing.

The strategy to take seismic imaging problems as generalized wave propagation phenomena may be applicable to other imaging problems, as well.

List of Figures

The photograph in fig. 4.14 was taken during a field measurement near Hagenbach/Südpfalz in Germany. I used it with the kind permission of Mr. Wolfgang Schott (DMT GeoTec).

DMT GeoTec – Geo-Engineering in Bochum, Germany is a business division of DMT – Gesellschaft für Forschung und Prüfung mbH, Essen, Germany, a subsidiary of the CUBIS group.

References

[Bel90] Michael Beleites. *Altlast Wismut. Ausnahmezustand, Umweltkatastrophe und das Sanierungsproblem im deutschen Uranbergbau.* Brandes und Apsel, Frankfurt, 1990.

[Gol89] S. V. Goldin. Method of discontinuities and theoretical problems of migration. In *59th Annual Internat. Mtg., Soc. Expl. Geophys., Expanded Abstracts*, volume 89, page 1326, 1989.

[Gol90] S. V. Goldin. A geometrical approach to seismic processing: The method of discontinuities. Technical Report 67, Stanford Exploration Project, 1990.

[Gol93] S. V. Goldin. A general theory of seismic imaging. In *55th Mtg. Eur. Assoc. Expl. Geophys., Abstracts*, volume 93, page Session:P119, 1993.

[Han95] Christian Hanitzsch. $AMIG$ *– Amplitude-preserving migration. Software package documentation*. Geophysical Institute, University of Karlsruhe, 1995.

[HST96] P. Hubral, J. Schleicher, and M. Tygel. A unified approach to 3-D seismic reflection imaging, Part I: Basic concepts. *Geophysics*, 61(3):742–758, 1996.

[HTS96] P. Hubral, M. Tygel, and J. Schleicher. Seismic image waves. *Geophys. Journ. Intern.*, 125:431–442, 1996.

[Hub77] Peter Hubral. Time migration - some ray theoretical aspects. *Geophys. Prosp.*, 25(4):738–745, 1977.

[JSH96] M. S. Jaya, J. Schleicher, and P. Hubral. Poststack time remigration. In *58th Mtg. Eur. Assoc. Expl. Geophys., Extended Abstracts*, 1996. Session X017.

[LB87] K. Larner and C. Beasley. Cascaded migrations - improving the accuracy of finite-difference migration *. *Geophysics*, 52(5):618–643, 1987.

[LH95a] F. Liptow and Peter Hubral. Migrating around in circles. *The Leading Edge*, 14(11):1125–1127, 1995.

[LH95b] Frank Liptow and Peter Hubral. Kinematic operators in seismic reflection imaging. In *57th Mtg. Eur. Assoc. Expl. Geophys., Extended Abstracts*, volume 95, Session P093, 1995.

[Man96] Jürgen Mann. Möglichkeiten der Ableitung räumlicher Verteilungen petrophysikalischer / bodenmechanischer Parameter aus hydroakustischen Meßdaten — Erster Zwischenbericht zum Studienauftrag vom 06.02.1996. Geophysical Institute, University of Karlsruhe, 1996.

[Man97a] Jürgen Mann. Möglichkeiten der Ableitung räumlicher Verteilungen petrophysikalischer / bodenmechanischer Parameter aus hydroakustischen Meßdaten — Zweiter Zwischenbericht zum Studienauftrag vom 06.02.1996. Geophysical Institute, University of Karlsruhe, 1997.

[Man97b] Jürgen Mann. Möglichkeiten der Ableitung räumlicher Verteilungen petrophysikalischer / bodenmechanischer Parameter aus hydroakustischen Meßdaten — Dritter Zwischenbericht zum Studienauftrag vom 06.02.1996. Geophysical Institute, University of Karlsruhe, 1997.

[MJ97a] Jürgen Mann and Makky S. Jaya. 3D finite-difference post-stack time and depth remigration. In *59th Mtg. Eur. Assoc. Expl. Geophys., Extended Abstracts*, Session A21, 1997.

[MJ97b] Jürgen Mann and Makky S. Jaya. Zeit- und Tiefenremigration in homogenen Geschwindigkeitsmodellen: Neuimplementierung und Anwendung auf synthetische Zero-Offset-Datensätze. In *57. Jahrestagung d. Deut. Geophys. Ges., Abstracts*, Session SK27, 1997.

[Pau91] Reimar Paul. *Das Wismut Erbe. Geschichte und Folgen des Uranbergbaus in Thüringen und Sachsen.* Die Werkstatt, Göttingen, 1991.

[PTVF86] W. H. Press, S. A. Teokolsky, W. T. Vetterling, and B. P. Flannery. *Numerical recipes in Fortran: The art of scientific computing.* Cambridge University Press, Cambridge, 1986.

[RLR85] D. H. Rothman, S. A. Levin, and F. Rocca. Residual migration - applications and limitations. *Geophysics*, 50(1):110–126, 1985.

[SMBN95] W. Schott, T. M. McGee, H. J. Boeck, and A. Neudert. High-resolution acoustic investigation of a mine tailings pond. In *Proceedings of 1st meeting of Environmental and Engineering Geophysics*, 1995.

[TSH94a] Martin Tygel, Jörg Schleicher, and Peter Hubral. Pulse distortion in depth migration *. *Geophysics*, 59(10):1561–1569, 1994.

[TSH94b] Martin Tygel, Jörg Schleicher, and Peter Hubral. Pulse distortion in depth migration. In *64th Annual Internat. Mtg., Soc. Expl. Geophys., Expanded Abstracts*, volume 94, pages 1359–1362, 1994.

[TSH96] M. Tygel, J. Schleicher, and P. Hubral. A unified approach to 3-D seismic reflection imaging, Part II: Theory. *Geophysics*, 61(3):759–775, 1996.

[Yil87] Özdogan Yilmaz. *Seismic data processing*. Soc. Expl. Geophys., Tulsa, 1987.

Appendix A

Derivation of the FD operators

If we take the Taylor expansion of a function $u(s)$ at s_0 and consider only terms up to the first order, we obtain an FD operator of first order for the first derivative of u:

$$u(s_0+h) = \sum_{n=0}^{\infty} \frac{h^n}{n!} \left.\frac{\partial^n u}{\partial s^n}\right|_{s_0} = u(s_0) + h \left.\frac{\partial u}{\partial s}\right|_{s_0} + o(h^2) \tag{A.1}$$

$$\Rightarrow \quad \left.\frac{\partial u}{\partial s}\right|_{s_0} \approx \frac{u(s_0+h)-u(s_0)}{h} \tag{A.2}$$

With the same ansatz and under consideration of terms up to the second order, we obtain the two following equations:

$$u(s_0+h) \approx u(s_0) + h \left.\frac{\partial u}{\partial s}\right|_{s_0} + \frac{h^2}{2} \left.\frac{\partial^2 u}{\partial s^2}\right|_{s_0} \tag{A.3}$$

$$u(s_0-h) \approx u(s_0) - h \left.\frac{\partial u}{\partial s}\right|_{s_0} + \frac{h^2}{2} \left.\frac{\partial^2 u}{\partial s^2}\right|_{s_0} \tag{A.4}$$

Adding the equations (A.3) and (A.4) yields an FD operator of second order for the second derivative of u:

$$\left.\frac{\partial^2 u}{\partial s^2}\right|_{s_0} \approx \frac{u(s_0-h)-2u(s_0)+u(s_0+h)}{h^2} \tag{A.5}$$

To find an FD operator of fourth order for the second derivative, we expand the following expressions up to the fourth order terms:

$$u(s_0+h) \approx u(s_0) + h \left.\frac{\partial u}{\partial s}\right|_{s_0} + \frac{h^2}{2} \left.\frac{\partial^2 u}{\partial s^2}\right|_{s_0} + \frac{h^3}{6} \left.\frac{\partial^3 u}{\partial s^3}\right|_{s_0} + \frac{h^4}{24} \left.\frac{\partial^4 u}{\partial s^4}\right|_{s_0} \tag{A.6}$$

$$u(s_0-h) \approx u(s_0) - h \left.\frac{\partial u}{\partial s}\right|_{s_0} + \frac{h^2}{2} \left.\frac{\partial^2 u}{\partial s^2}\right|_{s_0} - \frac{h^3}{6} \left.\frac{\partial^3 u}{\partial s^3}\right|_{s_0} + \frac{h^4}{24} \left.\frac{\partial^4 u}{\partial s^4}\right|_{s_0} \tag{A.7}$$

$$u(s_0+2h) \approx u(s_0) + 2h \left.\frac{\partial u}{\partial s}\right|_{s_0} + 2h^2 \left.\frac{\partial^2 u}{\partial s^2}\right|_{s_0} + \frac{4h^3}{3} \left.\frac{\partial^3 u}{\partial s^3}\right|_{s_0} + \frac{2h^4}{3} \left.\frac{\partial^4 u}{\partial s^4}\right|_{s_0} \tag{A.8}$$

$$u(s_0-2h) \approx u(s_0)-2h\left.\frac{\partial u}{\partial s}\right|_{s_0}+2h^2\left.\frac{\partial^2 u}{\partial s^2}\right|_{s_0}-\frac{4h^3}{3}\left.\frac{\partial^3 u}{\partial s^3}\right|_{s_0}+\frac{2h^4}{3}\left.\frac{\partial^4 u}{\partial s^4}\right|_{s_0} \quad \text{(A.9)}$$

Multiplying equations (A.6) and (A.7) by 16, adding them, and subtracting the equations (A.8) and (A.9), we eliminate $\frac{\partial^4 u}{\partial s^4}$. The discrete approximation for the second derivative now reads

$$\left.\frac{\partial^2 u}{\partial s^2}\right|_{s_0} \approx \frac{-u(s_0-2h)+16u(s_0-h)-30u(s_0)+16u(s_0+h)-u(s_0+2h)}{12h^2}. \quad \text{(A.10)}$$

Mixed derivatives can be calculated by approximating twice according to equation (A.2). For a function $v(s,t)$ this yields

$$\begin{aligned}\left.\frac{\partial^2 v}{\partial s\partial t}\right|_{(s_0,t_0)} &= \left.\frac{\partial}{\partial t}\left(\left.\frac{\partial v}{\partial s}\right|_{s_0}\right)\right|_{t_0} \\ &\approx \left.\frac{\partial}{\partial t}\left(\frac{v(s_0+h,t)-v(s_0,t)}{h}\right)\right|_{t_0} \\ &\approx \frac{v(s_0+h,t_0+k)-v(s_0+h,t_0)-v(s_0,t_0+k)+v(s_0,t_0)}{hk}\end{aligned} \quad \text{(A.11)}$$

as FD operator of first order.

Appendix B

Smoothing operator for the MZO

The numerical results in section 5.2 indicate the instability of the MZO under all tested conditions. After few offset steps we already obtain quickly increasing high frequency artifacts. The MZO process can be forced to be stable by introducing an additional smoothing operator. This operator is applied trace-by-trace after each offset step during the MZO process.

The smoothing operator has a width of $2\Delta t$ and computes for each sample a linear combination of this sample and its two nearest neighbours along each trace. The size of the operator is controlled by a parameter $0 \leq s \leq 1$. Its application corresponds to a convolution of each trace with a (possibly truncated) triangle or—for $s = 1$—with a rectangle, respectively. In fig. B.1 the operator is depicted for several values of s. Written as equation, the operator reads

$$\hat{p}^l_{i,j} = (s\,p^l_{i-1,j} + p^l_{i,j} + s\,p^l_{i+1,j})/(1+2s) \quad \forall\, i,j\,. \tag{B.1}$$

The smoothing operator has a strong impact on the stability of the MZO process. We were able to force the process to be stable under all tested conditions, but the smoothing also influences the calculated traveltimes. Due to this and due to the fact that the parameter s has to be determined for each application we consider this solution as quite unsatisfactory.

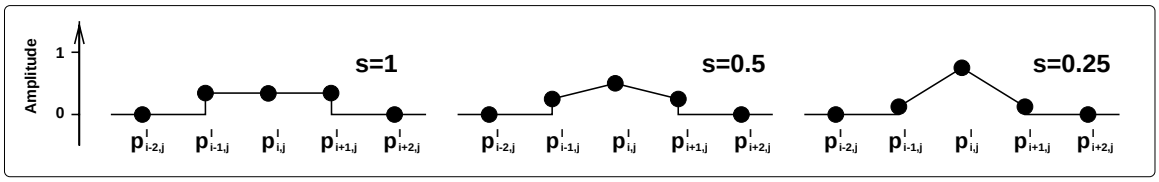

Figure B.1: Smoothing operator for different values of parameter s

Appendix C

Used hard- and software

We implemented the described programmes on a SILICON GRAPHICS POWER CHALLENGE L with IRIX 6.2 and presently 4 processors. Interactive applications were performed on SILICON GRAPHICS O2 workstations with IRIX 6.3 and HEWLETT PACKARD workstations series 700 with HP-UX 9.0.

In the beginning we used the language Ratfor, for the present implementations Fortran90. For parameter handling and data I/O we used programmes of the SEPlib package (Stanford Exploration Project).

For the 2D figures of the seismic data sets we used programmes of the Seismic Unix package (Center of Wave Phenomena at Colorado School of Mines). The 3D figures were generated with the Application Visualization System AVS (Advanced Visual Systems).

The analytic graphs in section 2 were created with own programmes written in the Interactive Data Language IDL (Research Systems). Programmes for the interpolation of data sets and for the scaling of 4D remigration results are also written in IDL.

Most of the shown synthetic data sets and the conventional migration results were generated with programmes of the Seismic Unix package. For additional synthetic data sets we used the $AMIG$ package [Han95].

This thesis was processed with LaTeX 2_ε including several extensions, the bibliography was generated with BibTeX .

Furthermore we utilized various own and public domain programmes which can hardly be enumerated in detail.

Appendix D

Acknowledgements

At first I would like to thank Prof. Dr. Peter Hubral and Prof. Dr. Sergei Shapiro, who considerably supported this work by their suggestions and their constructive critique.

I thank Dr. Makky S. Jaya for the intensive und fruitful cooperation, in particular in relation with the remigration problems.

Dipl.-Geophys. Wolfgang Schott and DMT GeoTec (see also page 71) decisively supported this work by providing real data sets and by offering the opportunity to work on a related study. In this context I also thank Dr. Xiao-Ping Li. He gave me a lot of advice related to technical and administrative affairs and initiated the related study mentioned above.

Finally I would like to thank all the colleagues at the Geophysical Institute who supported me in various ways with their critique, advise, programmes, reviewing etc.